NASA/TM—2002-211796

Characterization of the Temperature Capabilities of Advanced Disk Alloy ME3

Timothy P. Gabb and Jack Telesman
Glenn Research Center, Cleveland, Ohio

Peter T. Kantzos
Ohio Aerospace Institute, Brook Park, Ohio

Kenneth O'Connor
Glenn Research Center, Cleveland, Ohio

August 2002

The NASA STI Program Office . . . in Profile

Since its founding, NASA has been dedicated to the advancement of aeronautics and space science. The NASA Scientific and Technical Information (STI) Program Office plays a key part in helping NASA maintain this important role.

The NASA STI Program Office is operated by Langley Research Center, the Lead Center for NASA's scientific and technical information. The NASA STI Program Office provides access to the NASA STI Database, the largest collection of aeronautical and space science STI in the world. The Program Office is also NASA's institutional mechanism for disseminating the results of its research and development activities. These results are published by NASA in the NASA STI Report Series, which includes the following report types:

- TECHNICAL PUBLICATION. Reports of completed research or a major significant phase of research that present the results of NASA programs and include extensive data or theoretical analysis. Includes compilations of significant scientific and technical data and information deemed to be of continuing reference value. NASA's counterpart of peer-reviewed formal professional papers but has less stringent limitations on manuscript length and extent of graphic presentations.

- TECHNICAL MEMORANDUM. Scientific and technical findings that are preliminary or of specialized interest, e.g., quick release reports, working papers, and bibliographies that contain minimal annotation. Does not contain extensive analysis.

- CONTRACTOR REPORT. Scientific and technical findings by NASA-sponsored contractors and grantees.

- CONFERENCE PUBLICATION. Collected papers from scientific and technical conferences, symposia, seminars, or other meetings sponsored or cosponsored by NASA.

- SPECIAL PUBLICATION. Scientific, technical, or historical information from NASA programs, projects, and missions, often concerned with subjects having substantial public interest.

- TECHNICAL TRANSLATION. English-language translations of foreign scientific and technical material pertinent to NASA's mission.

Specialized services that complement the STI Program Office's diverse offerings include creating custom thesauri, building customized data bases, organizing and publishing research results . . . even providing videos.

For more information about the NASA STI Program Office, see the following:

- Access the NASA STI Program Home Page at ***http://www.sti.nasa.gov***

- E-mail your question via the Internet to help@sti.nasa.gov

- Fax your question to the NASA Access Help Desk at 301–621–0134

- Telephone the NASA Access Help Desk at 301–621–0390

- Write to:
  NASA Access Help Desk
  NASA Center for AeroSpace Information
  7121 Standard Drive
  Hanover, MD 21076

NASA/TM—2002-211796

Characterization of the Temperature Capabilities of Advanced Disk Alloy ME3

Timothy P. Gabb and Jack Telesman
Glenn Research Center, Cleveland, Ohio

Peter T. Kantzos
Ohio Aerospace Institute, Brook Park, Ohio

Kenneth O'Connor
Glenn Research Center, Cleveland, Ohio

National Aeronautics and
Space Administration

Glenn Research Center

August 2002

Acknowledgments

The authors gratefully acknowledge the support of the NASA GRC Ultra Efficient Engine Technology Program, managed by Robert J. Shaw, Ajay Misra, and Robert Draper. The support of the NASA GRC Materials Division and Structures Division, managed by Hugh Gray and James Kiraly, is also acknowledged. The authors also wish to acknowledge the many helpful discussions with Kenneth Bain, Jon Groh, Robert Vanstone, and David Mourer, General Electric Aircraft Engines, and Paul Reynolds, Pratt & Whitney. Subscale disk forgings and heat treatments were performed at Wyman-Gordon Forgings under the direction of William .

Available from

NASA Center for Aerospace Information
7121 Standard Drive
Hanover, MD 21076

National Technical Information Service
5285 Port Royal Road
Springfield, VA 22100

Available electronically at http://gltrs.grc.nasa.gov

Characterization of the Temperature Capabilities of Advanced Disk Alloy ME3

Timothy P. Gabb and Jack Telesman
National Aeronautics and Space Administration
Glenn Research Center
Cleveland, Ohio 44135

Peter T. Kantzos
Ohio Aerospace Institute
Brook Park, Ohio 44142

Kenneth O'Connor
National Aeronautics and Space Administration
Glenn Research Center
Cleveland, Ohio 44135

Abstract

The successful development of an advanced powder metallurgy disk alloy, ME3, was initiated in the NASA High Speed Research/Enabling Propulsion Materials (HSR/EPM) Compressor/Turbine Disk program in cooperation with General Electric Engine Company and Pratt & Whitney Aircraft Engines. This alloy was designed using statistical screening and optimization of composition and processing variables to have extended durability at 1200 °F in large disks. Disks of this alloy were produced at the conclusion of the program using a realistic scaled-up disk shape and processing to enable demonstration of these properties. The objective of the Ultra-Efficient Engine Technologies disk program was to assess the mechanical properties of these ME3 disks as functions of temperature, in order to estimate the maximum temperature capabilities of this advanced alloy. These disks were sectioned, machined into specimens, and extensively tested. Additional sub-scale disks and blanks were processed and selectively tested to explore the effects of several processing variations on mechanical properties. Results indicate the baseline ME3 alloy and process can produce 1300–1350 °F temperature capabilities, dependent on detailed disk and engine design property requirements.

Introduction

The advanced powder metallurgy disk alloy ME3 was designed in the NASA HSR/EPM disk program to have extended durability at 1200 °F in large disks. This was achieved by designing a disk alloy with moderately high γ' precipitate content and refractory element levels, optimized with supersolvus solution heat treatments to produce balanced monotonic, cyclic, and time-dependent mechanical properties. The resulting baseline alloy, processing, and supersolvus heat treatment has shown extended durability capabilities, combined with robust processing and manufacturing characteristics (ref. 1).

There is a long-term need for disks with higher rim temperature capabilities of 1300 °F or more. This would allow higher compressor exit (T3) temperatures and allow the full utilization of advanced combustor and airfoil concepts under development. The balance of mechanical properties necessary to achieve these temperature capabilities could vary with engine size and engine cycle design, as well as the particulars of a selected potential disk design and location in an engine. Such detailed preliminary and detailed design assessments are beyond the scope of this study. However, a general characterization of the mechanical properties of ME3 as functions of temperature would allow initial assessments of the balance of properties produced by the current baseline processing conditions and how these properties would impact such advanced applications.

The objective of this study was to assess the mechanical properties of ME3 as functions of temperature. This would enable assessments of the maximum temperature capabilities of this disk alloy for different potential applications in the engine community. Scaled-up disks processed in the HSR/EPM Compressor/Turbine Disk program were sectioned, machined into specimens, and extensively tested in tensile, creep, fatigue, and fatigue crack growth tests by NASA Glenn Research Center (GRC). Additional sub-scale material was processed and selectively tested to explore the effects of several processing variations on mechanical properties.

Materials and Procedure

Twelve scaled-up baseline ME3 disks were either subsolvus or supersolvus solution heat treated (ref. 1). They were then removed for brief fan air cooling followed by oil quenching. Subsequent stress relief heat treatment and aging heat treatment steps were then applied. These disks each had an outer diameter of near 24 in., maximum bore thickness of near 4 in., and rim thickness of near 2 in.

A remnant section of a scaled-up ME3 extrusion used for the scaled-up disks was machined to mults 3.5 in. dia. and 7 in. long, then forged into 15–20 pound sub-scale disks about 5–7 in. in diameter and 1.6 in. thick by Wyman-Gordon Forgings. Specimen blanks were machined using electro-discharge machining from one forging before heat treatment. The other disks were heat treated at Wyman-Gordon Forgings, Houston Div., Research & Development Shop. Solution heat treatment complexity and soak time effects were studied in the ME3 subscale disks and blanks. They were either given a simple, short "direct heatup" (DH) supersolvus heat treatment or a longer, two-step "pre-annealed" (PA) heat treatment sequence of subsolvus pre-anneal+ supersolvus solution heat treatment (ref. 2). Stress relief heat treatment and aging heat treatment steps were then applied to these two subscale disks. Two additional disks were given a DH solution heat treatment then a single step combined stress relief/aging (CSRA) heat treatment, designed using stress relaxation test data to be presented. The effects of the stress relief heat treatment step were further explored using subscale blanks. Selected blanks were given a stress relief heat treatment followed by the aging heat treatment, while other blanks were just directly aged after the solution heat treatment. Additional blanks were machined into stress relaxation specimens after just the solution heat treatment, in order to study stress relaxation occurring during potential stress relief and aging heat treatments.

It was intended that the subscale disks and blanks be quenched from the solution heat treatments at cooling rates typically expected at near-surface to deeply imbedded locations of large disks of several hundred pounds weight. Due to the much lower weight and volume of the subscale disks and blanks, this required design and screening of slower cooling procedures than typically employed for large disks. A procedure of fan air cooling starting 2 minutes after removal from the furnace was adopted for most of the subscale disks. An additional DH+CSRA disk was directly oil quenched starting 1 minute after removal from the furnace, to simulate faster cooling rates near the surfaces of large disks. The cooling procedure selected for the blanks was more complicated due to their very low mass and rapid cooling tendencies. A small resistance heating box furnace having a translating platform was used lower the blanks out of the hot zone at a controlled rate. The cooling temperature-time data of thermocouples embedded in the middle ("bore") and near the corner ("rim") of a subscale disk and in the middle of a blank are compared in Fig. 1. The temperature-time paths of cooling measured in the subscale disks was similar to that expected for large disks. The cooling path of the blanks closely reproduced that of the bore location of the subscale disks. The thermocouple temperature-time data recorded from 4 thermocouples embedded in one of the subscale disks during fan air and oil quenching cycles was analyzed using a commercial heat transfer computer code in order to assign approximate cooling rates, averaged over the temperature range of solution temperature to 1600 °F, for each extracted specimen.

An extensive mechanical testing matrix was employed for the scaled-up disks including tensile, notched tensile, creep, low cycle fatigue, and fatigue crack growth tests. Tensile tests were performed from 75 to 1500 °F on both supersolvus and subsolvus heat treated disk material. Other mechanical property tests were only performed on the supersolvus heat treated material. Stress relaxation tests were performed from 1400 to 1600 °F. Creep tests were performed from 1200 to 1500 °F. Low cycle fatigue tests were performed from 75 to 1400 °F. Cyclic crack growth tests were performed from 75 to 1500 °F, while dwell crack growth tests were performed from 1200 to 1400 °F. Mechanical test conditions of subscale disks and blanks were selected from among these conditions to allow direct comparisons with specimen tests from the scale-up disks.

Tensile Tests. Machining and testing of scaled-up disk tensile specimens was performed by Dickson Testing Company. Specimens having a gage diameter of 0.25 in. and gage length of 1.25 in. were machined and then tested in uniaxial test machines employing induction heating and axial extensometers. The tests were performed according to ASTM E21, using an initial test segment with strain increased at a uniform rate of 0.2%/min., followed by a segment with displacement increased at a uniform rate of 0.2 in./min. Tests of subscale material were performed at Dickson Testing Company and GRC on specimens machined by Metcut Research Associates having a gage diameter of 0.16 in. and gage length of 1 in. in a uniaxial test machine employing a resistance heating furnace and axial extensometer according to E21. Additional tensile specimens from subscale material were first subjected to exposures in air at 1400 and 1500 °F. About 0.020 in. was removed from the gage diameter of some of these specimens after exposures. Then all were tested at their exposure temperature. Notch tensile tests of specimens with a minimum gage diameter of 0.25 in. and notch stress concentration factor K_t =3.5 were performed at Dickson Testing Company according to E602.

Notched tensile tests of subscale material were performed at Dickson Testing Company and GRC on specimens machined by Metcut Research Associates having a minimum gage diameter of 0.16 in. and stress concentration factor K_t=3.5 in a uniaxial test machine.

Stress Relaxation Tests. Specimens having a gage diameter of 0.16 in. and gage length of 1 in. were machined from supersolvus solution heat treated subscale blanks and then tested at GRC in a uniaxial test machine employing resistance heating and an axial extensometer. The tests were performed in general accordance with E328, using an initial test segment having strain increased at a uniform rate of 0.2%/min., with the strain then held constant at 1.0% to allow stress relaxation for 8–24 hours.

Creep Tests. Machining of scaled-up disk creep specimens was performed by Metcut Research Associates. Specimens having a gage diameter of 0.25 in. and gage length of 1.5 in. were machined and tested in uniaxial lever arm constant load creep frames using resistance heating furnaces and shoulder-mounted extensometers. The creep tests were performed by GRC, Metcut, and Mar-Test, Inc. according to ASTM E139. Creep specimens of subscale material were machined and tested at Metcut. These specimens having a gage diameter of 0.16 in. and gage length of 0.75 in. were tested in constant load creep frames each using a resistance heating furnace and extensometer attached to the specimen gage section. Creep-rupture specimens of subscale disks having both a smooth gage section 0.16 in. diameter and 0.75 in. long, and a notched section of 0.16 in. notch dia. were machined by Metcut and tested at NASA GRC.

Low Cycle Fatigue Tests. Machining from scaled-up disks of low cycle fatigue specimens having gage diameters of 0.4 in. and gage lengths of 1.25 in. was performed by BITEC CNC Production Machining. The low cycle fatigue (LCF) specimens were then tested at Mar-Test, Inc. using uniaxial closed-loop servo-hydraulic testing machines with induction heating and axial extensometers. Tests were performed according to ASTM E606. A frequency of 0.5 hertz was employed in strain-controlled fatigue testing for the first 24 hours of cycling. Strain ratios ($R_\varepsilon=\varepsilon_{max}/\varepsilon_{min}$) of 0.5, 0, and –1 were used. Surviving specimens were then cycled to the same stabilized stresses using a load-controlled cycle at a faster frequency of 5 hertz until failure. LCF specimens having gage diameters of 0.25 in. and gage lengths of 0.75 in. were machined from the subscale disks by BITEC and tested at Mar-Test, Inc. using the same procedures. Additional LCF specimens from subscale material were first subjected to exposure in air at 1400 °F for 500h. They were then all tested at 1400 °F.

Fatigue Crack Growth Tests. Machining of surface flaw fatigue crack growth specimens (ref. 3) from scaled-up disks was performed by Low Stress Grind, Inc. Machining of specimens of the same configuration from subscale disks was performed by BITEC. All specimens had a rectangular gage section 0.4 in. wide and 0.18 in. thick, with a surface flaw about 0.014 in. wide and 0.007 in. deep produced by electro-discharge machining. The fatigue crack growth specimens were then tested at NASA GRC. Tests were performed in a closed-loop servohydraulic test machine using resistance heating and potential drop measurement of crack growth. Pre-cracking was performed at room temperature. Tests were then performed at elevated temperatures using a maximum stress of 100 ksi. Cyclic tests were performed at a frequency of 0.33 hertz. Various stress ratios ($R_\sigma=\sigma_{min}/\sigma_{max}$) were used in the cyclic tests. Dwell tests

were performed with various times of dwelling at maximum stress in each cycle, using stress ratios of 0 or 0.05.

Fracture surfaces of selected specimens were evaluated by scanning electron microscopy. Cracking modes and grain sizes were also examined on metallographically prepared sections. Grain sizes were determined according to ASTM E112 linear intercept procedures using circular grid overlays, and As-Large-As (ALA) grain sizes were determined using ASTM E930.

Results and Discussion

Typical Microstructures

Typical grain microstructures in optical images of etched metallographic sections of tensile specimen grip sections are shown in Fig. 2. These tensile specimens were from the disks' rim regions, which cooled more quickly during quenching than the bore sections. Supersolvus heat treated scaled-up material had a mean grain size of ASTM 7.1 (27.5 μm), with a standard deviation of ASTM 0.2 (2.0 μm) and ALA grain size rating of ASTM 3.25. Subsolvus heat treated scaled-up material had a mean grain size of ASTM 12.0+/-0.1 (5+/-0.2 μm) and ALA grain size of ASTM 8. Typical γ' precipitate microstructures in transmission electron microscopy superlattice darkfield images from thinned foils of tensile specimen grip sections are also shown in Fig. 2. Within the grains of supersolvus specimens, three populations of γ' precipitates were evident. Scattered large precipitates (0.3–0.5 μm diameter) appeared to have preferentially grown at the cube corners, giving consistently oriented star shapes. Selected area diffraction pattern analyses indicated the cube sides corresponded to {001} planes, while the extended cube corners grew out in <111> directions, as previously reported elsewhere (ref. 4). Intermediate size precipitates (0.15–0.3 μm diameter) had a simpler, rounded cube shape. Fine precipitates (0.01–0.05 μm diameter) were spherical.

Subsolvus specimens had less distinct differences in large versus intermediate precipitate morphology and size ranges, but still displayed some evidence of preferential growth at the cube corners. The fine spherical precipitates were somewhat smaller in subsolvus specimens. Coarse, undissolved "primary" γ' particles (0.6–2 μm in diameter) were spaced along grain boundaries and sometimes widely scattered within grains.

Tensile Stress-Strain Response

The stress-strain curves of typical tensile tests are shown in Figs. 3–4. Both supersolvus and subsolvus specimens had serrated plastic flow at intermediate temperatures, peaking at 800 °F then subsiding at higher temperatures. At temperatures of 1400 °F and higher, initial peak strengths were usually attained at the slow initial testing strain rate, followed by plastic softening to lower stresses. These tests then generated higher stresses and a higher ultimate strength when switched to a faster constant displacement rate in the second test segment, as shown in Figs. 3–4. This indicated that the strength was strain rate dependent, and decreased with decreasing strain rate at these temperatures. This variation of strength with strain rate is not usually encountered in current disks which run at lower temperatures, and such strength variations could present design challenges at these higher temperatures. The strain rate

sensitivity (m) of strength for these temperatures was estimated by linear regression using the general equation (ref. 5):

$$\sigma = K'(d\varepsilon/dt)m \; ; \; \log \sigma = \log K' + m \log(d\varepsilon/dt)$$

Strain rate sensitivity increased with temperature, and tended to be slightly higher for subsolvus material than supersolvus material, as shown in Fig. 5. Yield strengths at 0.2% offset, ultimate strengths, notched strength, % elongation after failure, and % reduction in area after failure are compared as functions of temperature in Figs. 6–8. Polynomial regression was performed on these responses using temperature (T), T^2, and T^3 as the independent variables. The resulting equations and correlation coefficients are listed in the figures, for use in estimating mean strengths and ductilities. Yield strength was sustained to a temperature of 1300 °F, then dropped off with increasing temperature. Ultimate strength began dropping off above 1200 °F. Specimens extracted from the disk rims usually had higher strengths than those from disk bores, possibly due to the higher cooling rates expected in rims (ref. 6). Elongation and reduction in area did not significantly vary as functions of temperature for supersolvus heat treated material.

Test results of specimens from supersolvus heat treated subscale disks and blanks are shown in Figs. 9–14. The subscale material had comparable tensile properties to the baseline scaled-up disks, for the DH and PA solution heat treatments with baseline stress relief plus aging heat treatments. The blanks given the standard aging heat treatment without the stress relief step also had comparable response. The DH solution with CSRA combined stress relief/aging heat treatments gave 5–10 ksi higher strength at the highest temperatures than the scaled-up disk specimens, with the oil quenched subscale disk giving highest strengths.

Yield and ultimate strength of the subscale disk specimens are shown versus approximate cooling rate in Fig. 14. Increasing cooling rate consistently increased strength, as previously reported (ref. 6). Yield strength was usually more strongly increased by cooling rate than ultimate strength. The effects generally decreased with increasing test temperature from 1100 °F to 1500 °F. Simple linear regression equations are included for estimating cooling rate effects on mean response.

The tensile properties of this alloy could be affected by service time at the projected advanced disk operating temperatures of 1400 °F and higher. In order to briefly assess these effects, groups of fully machined tensile specimens were exposed at 1400 °F/500 h and 1500 °F/600 h. The gage sections of some of the specimens were re-machined after exposure to remove the oxidized surface layer, then all specimens were tensile tested at their exposure temperatures. The resulting yield strengths, ultimate strengths, elongations, and reductions in area are compared for specimens of low and high average cooling rates in Fig. 15. After 1400 °F/500 h exposure, yield strength was reduced by less than 5 ksi while ultimate strength was increased by 3–5 ksi. There was no consistent effect on reduction in area, and machining away the oxidized surface layer did not consistently change these results. These results suggest that extended service at 1400 °F would not substantially degrade strength or ductility due to volume-dependent microstructural effects or near-surface oxidation effects.

After 1500 °F/600 h, yield strength was reduced by 15–25 ksi, while ultimate strength was reduced by 13–20 ksi. The strength effects were greater for material having

slow (near 112 °F/min) average cooling rates. Machining away the oxidized surface layer increased exposed strengths by only 2–3 ksi. Reduction in area after this exposure was more sharply reduced to 30–50% of unexposed values. The effects on ductility were greater for material having fast (near 160 °F/min) average cooling rates. Machining away the oxidized surface layer increased reduction in area of exposed specimens to 50–75% of unexposed values. These results suggest that extended service at 1500 °F could sharply reduce strength primarily due to volume-dependent microstructural effects, and sharply reduce near-surface ductility due to oxidation as well as microstructural effects.

Typical tensile fracture surfaces are compared in Fig. 16. Tensile specimens had a predominantly transgranular failure mode by microvoid coalescence in tests from room temperature to 1300 °F. At intermediate temperatures, scattered slip "facet" grain failures were also observed. At higher temperatures of 1400–1500 °F, oxidized intergranular surface cracks appeared to precede the transgranular microvoid coalescence.

Stress Relaxation Response

Stress versus time in typical stress relaxation tests at 1400 to 1600 °F are shown in Fig. 17. The rate of stress relaxation decreased with increasing time, such that stress decreased linearly with log(time). Relaxation increased with increasing temperature as expected. Multiple linear regression was performed on stress versus log (time) and temperature (P-to-enter=0.05). The resulting equation and correlation coefficient are listed in the figure, for use in estimating mean stress relaxation response. This equation showed the strong temperature dependence of stress relaxation, and indicated the temperature dependence was enhanced at higher values of log(time). These results indicated a combined stress relief/aging (CSRA) heat treatment of 1500 °F/8 h could relax residual stresses from quenching to below 50 ksi, judged sufficient in this study. Expected variations in time at this stress relief temperature due to production batching and disk section-size effects, estimated to be at least +/- 1h, were predicted to produce only minor variations in resulting residual stresses for this CSRA combined stress relief/aging heat treatment.

Creep Properties

Creep strain-time curves of typical creep tests lasting over 1400 h at 1200, 1300, 1400, and 1500 °F are shown in Fig. 18. Creep data was generated for tests extending from 1h to over 10,000 h in some cases. Tests at higher temperature tended to have smaller periods of primary creep, and larger periods of tertiary creep. Times to 0.1%, 0.2%, 0.5% and rupture were first analyzed using a Larson-Miller approach (ref. 7) commonly employed for disk alloys. Creep results were used to generate conventional Larson-Miller curves of stress versus Larson-Miller parameter (LMP) using the equation:

$$LMP=(T+460°R)(\log t + C)$$

The resulting plots are shown in Figs. 19–22. It can be seen that the LMP constant C=20 did not fully account for test temperature in modeling the time to produce low creep strains of 0.1, 0.2%, or 0.5%, but worked well for rupture life. Regressions indicated a constant of 28 gave the best compromise of high correlations for 0.1%, 0.2%, and 0.5%. Polynomial regression equations using the variables LMP and LMP^2 are included with

correlation coefficients in the figures, for use in estimating mean life responses as functions of temperature and stress using this Larson-Miller approach.

Times to 0.2% creep are also compared for test temperatures of 1200–1500 °F in Fig. 23. A simpler approach using multiple quadratic regression was performed to model time to 0.2% creep, using stress, temperature and their resulting interactions. The resulting equation and correlation coefficient is also given, for directly estimating mean response.

Test results of specimens from subscale pancakes and blanks are compared to the scale-up results in Fig. 24. The subscale material did have comparable creep properties to the scaled-up disks. The creep properties did not significantly vary between the DH and PA solution heat treatments, however creep resistance varied when the stabilization heat treatment step was removed. Creep life at 1200 °F/125 ksi and 1400 °F/60 ksi significantly increased when the stress relief step was removed from the baseline SR+A cycle, Fig. 25. Significantly more scatter in life was apparent in the subscale data than scaled-up data. This was apparently due to extensometer slipping for the small specimen configuration used for the DH+SR+A and PA+SR+A material. Small extensometers were lightly attached to the gages of these small specimens, while larger extensometers were more firmly attached to ridges on the shoulders of larger specimens. Specimens were machined from the subscale CSRA disks using the larger specimen configuration, as in the scaled-up material tests. The resulting 0.2% lives exhibited much lower scatter which was comparable to the scaled-up data, and slightly exceeded scaled-up lives at both 1300 and 1500 °F.

Times to 0.2% creep of the subscale DH+CSRA disk specimens are shown versus approximate cooling rate in Fig. 26. Increased cooling rate improved creep life at lower temperatures (1300 °F/100 ksi), but reduced creep life at high temperatures (1500 °F/50 ksi). The effects on creep life were less than 2X for both cases, over the range of cooling rates evaluated.

Creep specimens tended to fail from intergranular, surface-initiated cracks at all creep test temperatures, as shown in Fig. 27. Specimens tested at higher stress levels had fewer cracks than those tested at lower stresses, for each test temperature. At increasing temperatures of 1400–1500 °F, exposed grain surfaces on the surface cracks had a more rough, dimpled morphology and more secondary cracking, with evident grain boundary cavitation. The final overload failure occurred by transgranular microvoid coalescence with scattered “facet” grain failures at 1200 °F. At increasing temperatures of 1300–1500 °F, the final overload failures increasingly favored cavitation at grain boundaries.

Low Cycle Fatigue Properties

Total strain range versus life is compared for the test temperatures at each strain ratio of 0.5, 0, and –1 in Fig. 28. Fatigue lives at 75, 1000 °F, and 1400 °F are shown as functions of strain range and strain ratio (R_ε) in Fig. 29. A generalized polynomial regression using temperature as a variable along with strain range and strain ratio gave unsatisfactory results, with large error. Regressions at each temperature were therefore performed using strain range, R_ε, and their interactions. The resulting equations and correlation coefficients are included in the figure. The effects of strain ratio were found to increase with temperature. The effect of strain ratio was quite modest at 75 °F, with higher strain ratios reducing life by less than about 80%. However, both strain ratio and

the interaction between strain ratio and strain range became more significant along with strain range at the higher temperatures of 1000 and 1400 °F. At these temperatures, higher strain ratios reduced life by over 90%. The resulting equations are included in Fig. 29 for estimating mean life responses at these temperatures.

Close inspection of Fig. 28 indicates fatigue life for low strain ranges was lower in tests at 400–800 °F than at room temperature and higher temperatures up to 1400 °F. This is shown in Fig. 30 comparing lives at strain ranges of 0.55 and 0.70% with a strain ratio of 0. Simple polynomial regression equations using T and T^2 are included in this figure, for use in estimating mean life responses for these conditions as a function of temperature.

Test results of specimens from subscale disks are compared to the scaled-up results in Fig. 31. Groups of six tests were run at the temperatures of 800 and 1400 °F using a strain range of 0.55%, R_ε=0. The subscale material had comparable fatigue resistance to the scaled-up disks. The fatigue properties did not significantly vary between the DH and PA solution heat treatments. These results did confirm that mean life, given at a cumulative probability of 50%, was lower at 800 °F than that at 1400 °F.

Six additional specimens from subscale disks were given a prior exposure in air at 1400 °F for 500 h before LCF testing at a strain range of 0.55%, R_ε=0, in order to briefly screen the effects of realistic service exposure times. These results are also compared in Fig. 32. The mean life was similar to the unexposed mean life. However, a single exposed specimen failed at only 5% of the mean cyclic life of the other five. A dissimilar surface initiated failure mode was responsible for the low life of this exposed specimen, as will be discussed below.

Low cycle fatigue specimens predominantly failed from cracks initiated by planar failure of relatively large grains from room temperature to 1400 °F, as shown in Fig. 33. These "faceted" grain failures appeared to be due to concentrated slip on {111} planes, which could produce slip offsets in large grains, ref. 8. The grain facets were most flat with least texture in tests at 400 and 800 °F. The grain facets had more texture in tests at room temperature and 1000–1400 °F. More cracks were initiated in tests at higher strain ranges and higher strain ratios. A smaller number of specimens failed from oxidized surface cracks. These cracks were either transgranular or intergranular. A much smaller minority of specimens failed from ceramic inclusions. The inclusions were more often granulated alumina inclusions often referred to as Type 2 soft, reactive inclusions (ref. 9).

Among fatigue specimens pre-exposed at 1400 °F/500 h, the five specimens having long mean life failed from internal cracks initiated at facets or inclusions, as typified in Fig. 34. The single specimen failing at a much lower life had a surface initiated failure with intergranular cracking. Evaluation of a metallographic section of this specimen prepared transverse to the loading axis indicated general oxidation damage along the specimen surface, producing an outer layer of NiO and underlying branches rich in Al_20_3 extending further in, as shown in Fig. 35. The alumina-rich branches grew in at grain boundaries as well as along the machined grain surface. The activation of this crack initiation mode at surface oxidation during service at 1400 °F could present significant fatigue design challenges, due to the 10X lower fatigue life of the exposed specimen with this failure mode. This failure mode has been shown to be operative after prior exposures as well as during extended cycle periods in another powder metallurgy

superalloy, Udimet 720, at temperatures as low as 1200 °F (ref. 10). Cyclic life was reduced by up to 8X in that work.

Fatigue Crack Growth Properties

Cyclic crack growth rate versus stress intensity factor range is compared for all test temperatures at stress ratios (R_σ) of –0.5 and 0.25 in Fig. 36. Crack growth rates increased with temperature at both negative and positive stress ratios, and increased with increasing stress ratio. The increase in crack growth rates with temperature was quite modest, increasing roughly 8–10X in going from 75 to 1200 °F. This is shown more clearly in Fig. 37, comparing cyclic crack growth rates at a fixed stress intensity factor range versus temperature. Linear regression equations modeling cyclic crack growth rates versus temperature are included in this figure, for use in estimating mean crack growth responses as a function of temperature.

Dwell crack growth rate versus stress intensity factor range is compared for all test temperatures at each stress ratio of 0 and 0.05 in Fig. 38. Most notable is the wide scatter in dwell crack growth rates at each temperature. This was found to be related to cooling rate, with specimens from higher cooling rate rim locations having higher crack growth rates than slow cooling rate bore locations. Test results and linear regression equations modeling dwell crack growth rates at maximum stress intensities of 25 $ksi*in^{0.5}$ and 30 $ksi*in^{0.5}$ versus temperature are included in Fig. 39, for use in estimating mean crack growth responses as a function of temperature.

Dwell crack growth rate versus estimated average cooling rate of specimens from DH&PA+SR+A subscale pancakes are shown in Fig. 40. Dwell crack growth rates were shown to increase by over 10X when going from slowest (116 °F/min) to fastest cooled (168 °F/min) specimens at 1300 °F. The crack growth rate increase with cooling rate was reduced to 5X at 1400 °F. The subscale material did have comparable crack growth properties to the specimens from the scaled-up disks, the latter specimens extracted from relatively fast cooled disk rim regions. The cyclic and dwell crack growth properties did not significantly vary between the DH and PA solution heat treatments.

The cracking mode observed in fatigue crack growth tests varied most notably between the cyclic and dwell tests. Cyclic crack growth specimens had majority transgranular cracking at all test temperatures, Fig. 41. While the proportion of transgranular cracking was essentially 100% at 75 °F, an increasing percentage of intergranular cracking became apparent at temperatures of 1200°F and higher. Specimens tested from 75 to 1200 °F displayed planar cracking of some individual grains by facet failure, possibly related to concentrated slip on {111} planes as for the low cycle fatigue specimens. At higher temperatures a more textured fracture morphology was observed which was more nearly Mode 2.

Dwell crack growth specimens had predominantly intergranular cracking at the temperatures tested, Fig. 42, as previously observed in other superalloys in dwell crack growth tests (refs. 11–12). The intergranular cracking mode was mixed with minor trangranular cracking in tests of short dwell times and lower temperatures of 1200 °F. These exposed grain boundaries were relatively flat. However, the intergranular failure became highly prevalent in tests at higher temperatures, with considerable secondary grain boundary cracks obvious. The exposed grain surfaces had large dimples due to cavitation.

Summary and Conclusions

Scaled-up ME3 disks processed in the HSR/EPM disk program were sectioned, machined into specimens, and mechanically tested. Additional sub-scale disks and blanks were processed and tested to explore the effects of several processing variations on mechanical properties. Scaled-up disks had quite comparable mechanical response to sub-scale disks, for common test conditions where direct comparisons were possible. The mechanical properties of ME3 can be summarized as follows:

1) Tensile: Scaled-up ME3 had stable tensile strength and ductility to at least 1300 °F. Strength generally increased with increasing cooling rate, however this effect decreased with increasing temperature. Strength became strain rate dependent at 1400 °F, decreasing with decreasing strain rate. Strength and ductility also became exposure time dependent at 1500 °F, decreasing with increasing exposure time. Microvoid coalescence within grains produced failure at 75–1300 °F, but surface cracking interceded at 1400–1500 °F.
2) Stress relaxation: Stress relaxation increased with increasing log(time) and temperature, and was accentuated at high temperatures and long times. A combined stress relaxation + aging heat treatment could be designed using stress relaxation test results.
3) Creep: ME3 would creep less than 0.2% in 100h at 1300 °F with an applied stress of 100 ksi. At 1400 °F and 1500 °F, this applied stress dropped drastically to about 75 ksi and 50 ksi, respectively. Creep response could be modeled versus temperature and stress using simple regression. Alternatively, a Larson-Miller Parameter approach using a Larson Miller constant of 28 worked well for low creep strains, while a constant of 20 worked well for rupture. Intergranular surface cracking limited rupture life at all test temperatures.
4) Low cycle fatigue: At strain ranges of 0.7% or less typically encountered in applications, ME3 had good LCF resistance up to 1400 °F. However, at higher strain ranges, life decreased at 1400 °F due to decreasing strength. Extended exposures at 1400 °F could also reduce life at low strain ranges by up to 20X. Slip failures of large grains initiated failure at most temperatures. However, some failures at 1400 °F were produced by crack initiation modes at surface oxidation.
5) Crack growth: Cyclic crack growth rates only increased by 12X between 75 °F and 1300 °F. However, dwell crack growth rates strongly increased with temperature from 1200 to 1500 °F, by about 10X per 100 °F. Dwell crack growth rates also strongly increased with increasing cooling rate at 1300 °F, although this effect appeared reduced at 1400 °F.

It can be concluded from this evaluation that ME3 has at least 1300 °F general capabilities. Potential maximum temperatures for consideration in detailed assessments of potential applications can also be suggested according to each property:

1) Tensile: 1250–1300 °F based on yield and ultimate strength needs in disk bores and webs.
2) Creep: 1300–1400 °F based on 100–75 ksi creep stress requirements in webs and rims.

3) Low cycle fatigue: 1300–1400 °F based on strain and service exposure requirements throughout the disk.
4) Fatigue crack growth: 1300–1400 °F based on dwell crack propagation in limiting rim locations.

References

1. T.P. Gabb, J. Gayda, J. Telesman, "Development of Advanced Powder Metallurgy Disk Alloys in NASA-Industry Programs," Aeromat 2001, Long Beach, CA, June 14, 2001.
2. C.P. Blankenship, M.F. Henry, J.M. Hyzak, R.B. Rohling, E.L. Hall, "Hot-Die Forging of P/M Ni-Base Superalloys," Superalloys 1996 , ed. R.D. Kissinger, D.J. Deye, D.L. Anton, A.D. Cetel, M.V. Nathal, T.M. Pollock, D.A. Woodford, TMS, Warrendale, PA, 1996, pp. 653–662.
3. R.H. Vanstone, T.L. Richardson, "Potential-Drop Monitoring of Cracks in Surface-Flawed Specimens," ASTM STP 877, American Society for Testing and Materials, W. Conshohocken, PA, 1985, 148–166.
4. R.A. Ricks, A.J. Porter, R.C. Ecob, "The Growth of γ′ Precipitates in Nickel-Base Superalloy," Acta. Met., V. 31, 1983, pp. 43–53.
5. W.F. Hosford, R.M. Caddell, Metal Forming Mechanics and Metallurgy, Prentice-Hall, Englewood Cliffs, NJ, 1983, pp. 80–81.
6. J.E. Groh, "Effect of Cooling Rate From Solution Heat Treatment on Waspaloy Microstructure and Properties," Superalloys 1996 , ed. R.D. Kissinger, D.J. Deye, D.L. Anton, A.D. Cetel, M.V. Nathal, T.M. Pollock, D.A. Woodford, TMS, Warrendale, PA, 1996, pp. 621–626.
7. F.R. Larson, J. Miller, Trans. ASME, V. 74, 1952, pp. 765–766.
8. T.P. Gabb, J. Gayda, J. Sweeney, "The Effect of Boron on the Low Cycle Fatigue Behavior of Disk Alloy KM4," NASA/TM—2000-210458, NASA, Washington, D.C., 2000.
9. D.R. Chang, D.D. Krueger, R.A. Sprague, "Superalloy Powder Processing , Properties, and Turbine Disk Applications," Superalloys 1984, ed. M. Gell, C.S. Kortovich, R.H. Bricknell, W.B. Kent, J.F. Radavich, TMS, Warrendale, PA, pp. 245–252.
10. T.P. Gabb, J. Telesman, P.T. Kantzos, J.W. Sweeney, P.F. Browning, "Effects of High Temperature Exposures on Fatigue Life of U720," Fatigue-David L. Davidson Symposium, ed. K.S. Chan, P.K. Liaw, R.S. Bellows, T.C. Zogas, W.O. Soboyejo, TMS, 2002, pp. 261–269.
11. K.R. Bain, M.L. Gambone, J.M. Hyzak, M.C. Thomas, "Development of Damage Tolerant Microstructures in Udimet 720," Superalloys 1988, ed. S. Reichman, D.N. Duh., G. Maurer, S. Antolovich, C. Lund, TMS, 1988, pp. 13–22.
12. J. Gayda, T.P. Gabb, R.V. Miner, "Fatigue Crack Propagation of Nickel-Base Superalloys at 650 °C," Low Cycle Fatigue, ASTM STP 942, ed. H.D. Solomon, G.R. Halford, L.R. Kaisand, B.N. Leis, ASTM, Philadelphia, PA, 1988, pp. 293–309.

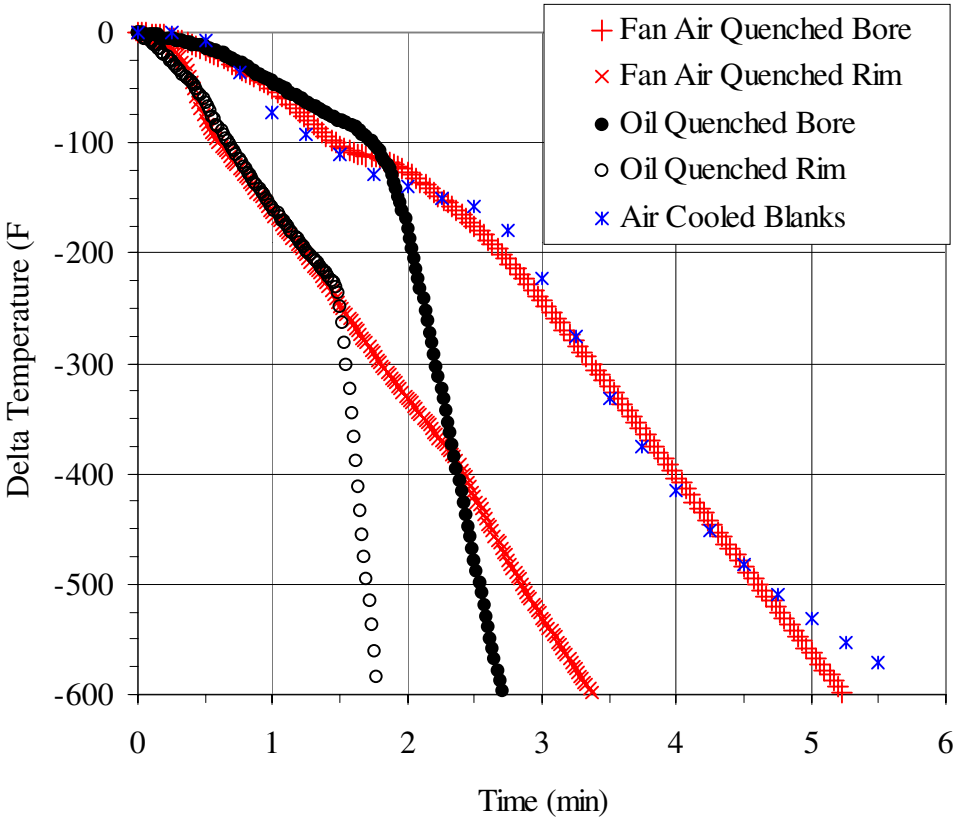

Fig. 1. Temperature versus time for thermocouples in the mid section (bore) and corner (rim) of subscale disks during fan air and oil quenching, compared to thermocouple data from air cooled blanks.

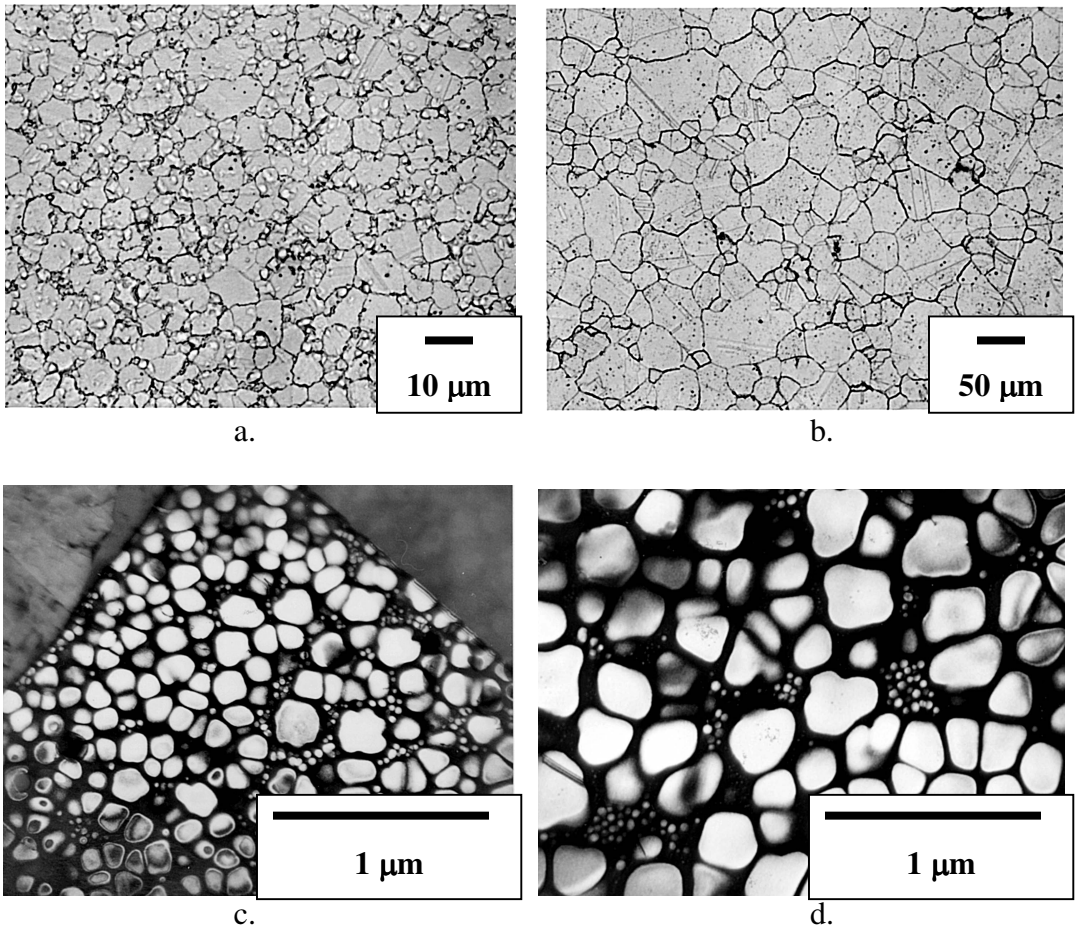

Fig. 2. Typical microstructures of scaled-up disks: a. subsolvus heat treated disk, S001 rim grain structure; b. supersolvus heat treated disk, S101 rim grain structure; c. S001 rim γ′microstructure; d. S101 rim γ′microstructure.

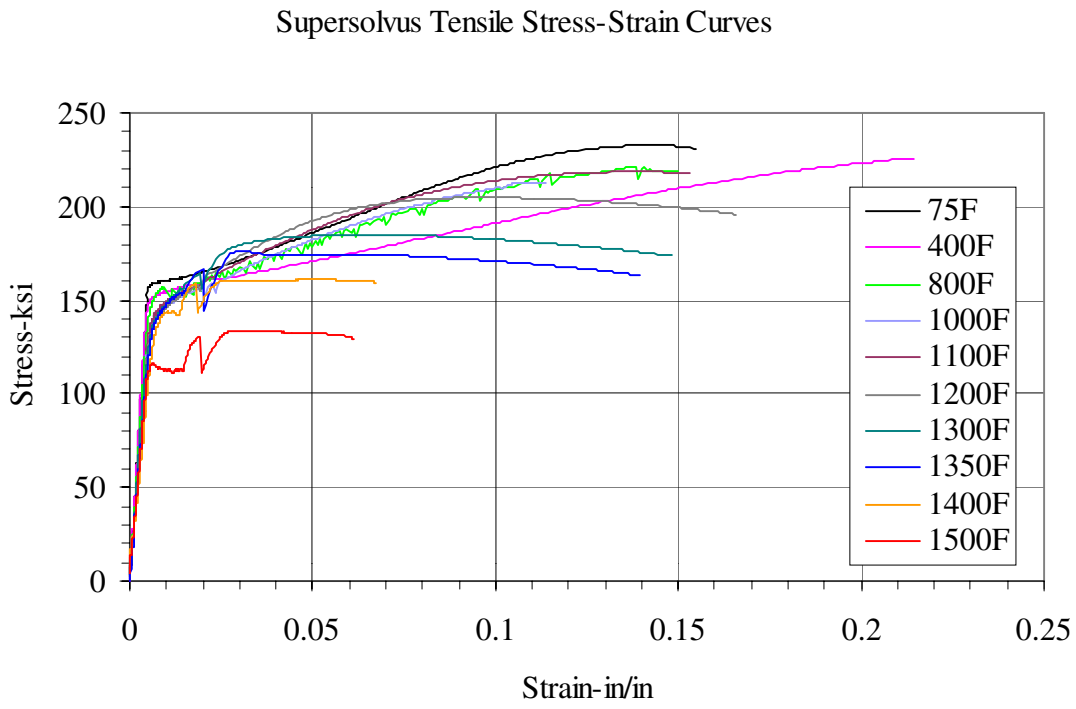

a.

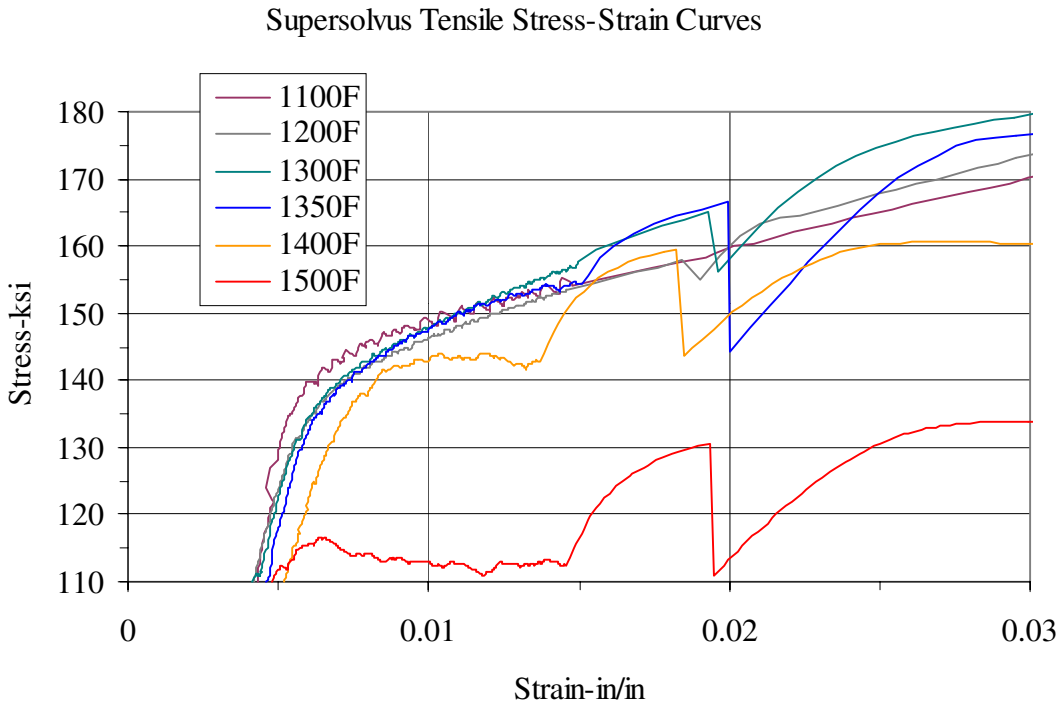

b.

Fig. 3. Typical tensile stress-strain curves from supersolvus scaled-up disks, a) entire test, b) initial stages at high temperature.

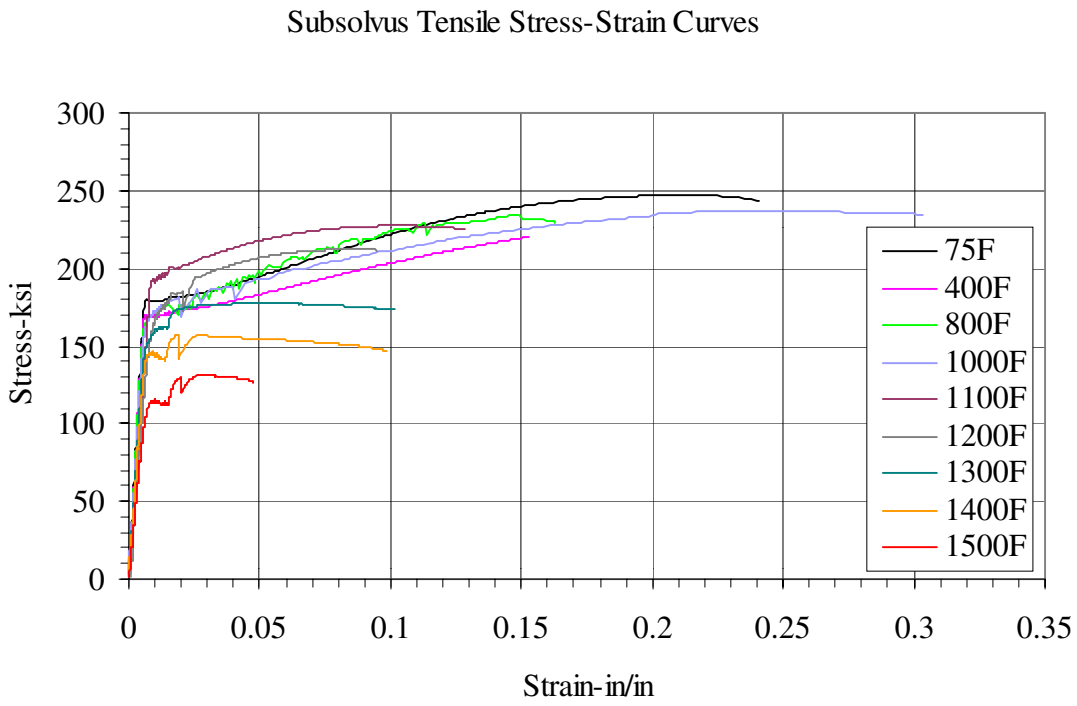

a.

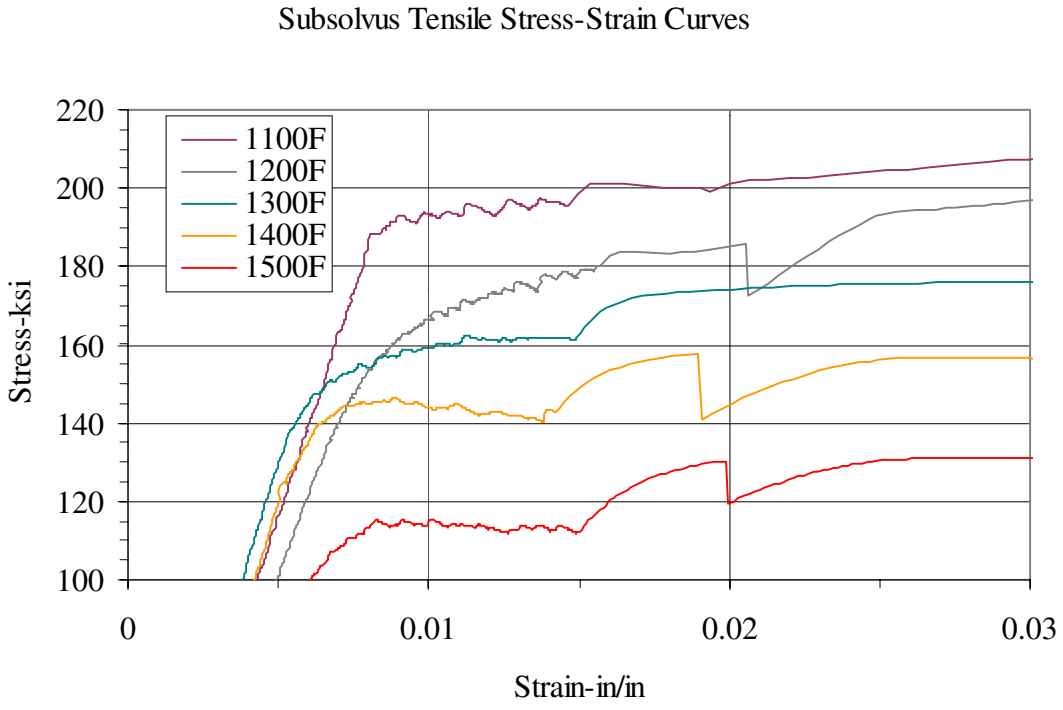

b.

Fig. 4. Typical tensile stress-strain curves from subsolvus scaled-up disks, a) entire test, b) initial stages at high temperature.

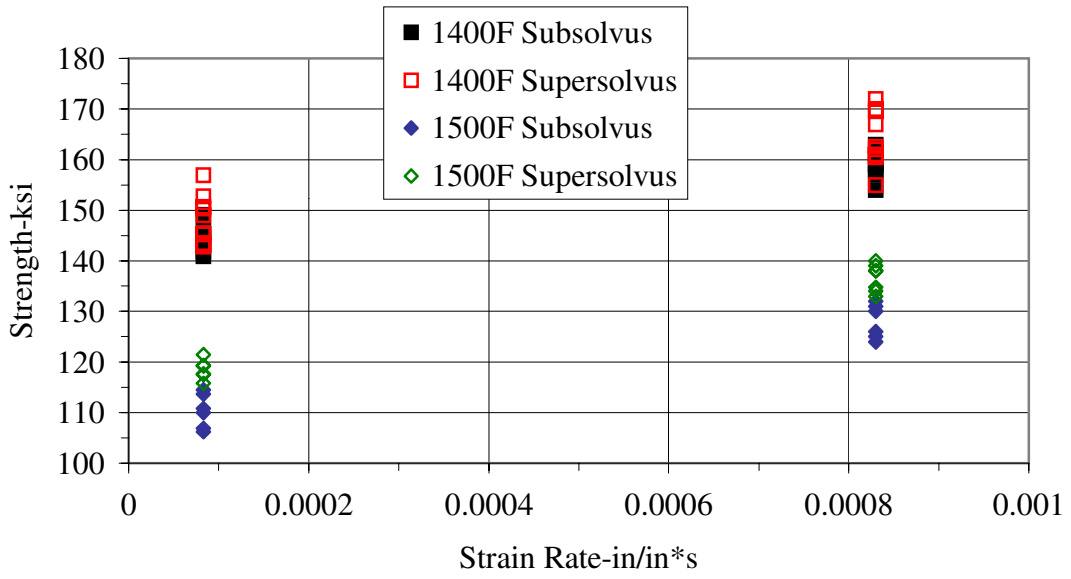

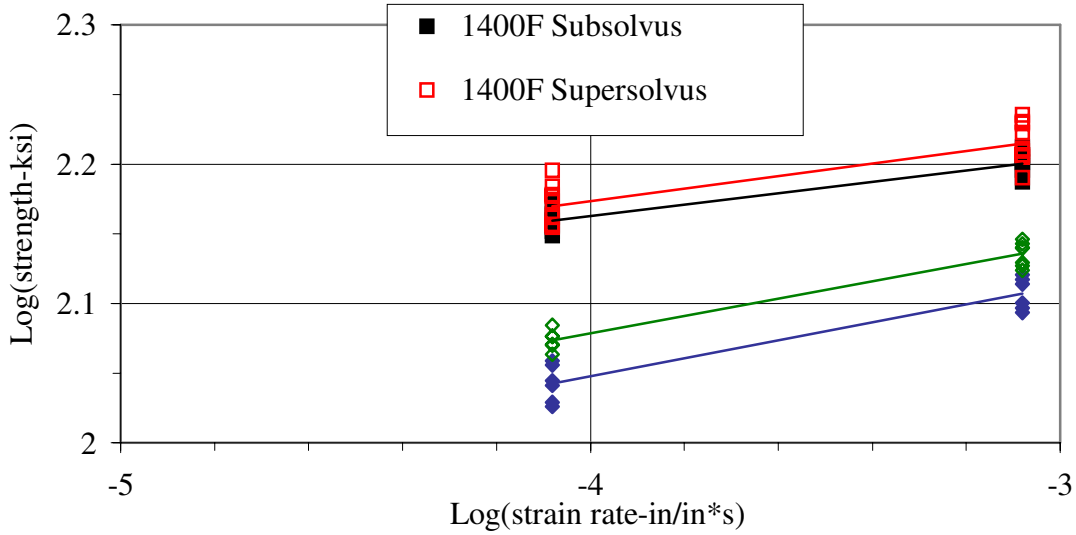

Sup. 1400F $\log(\sigma) = 0.0448*\log(d\varepsilon/dt) + 2.3527$

$R^2 = 0.7406$

Sub. 1400F $\log(\sigma) = 0.0411*\log(d\varepsilon/dt) + 2.327$

$R^2 = 0.8835$

Sup. 1500F $\log(\sigma) = 0.062*\log(d\varepsilon/dt) + 2.3267$

$R^2 = 0.9469$

Sub. 1500F $\log(\sigma) = 0.0645*\log(d\varepsilon/dt) + 2.3057$

$R^2 = 0.8885$

Fig. 5. Strain rate dependence of strength at 1400 and 1500 °F shown using normal and logarithmic axes.

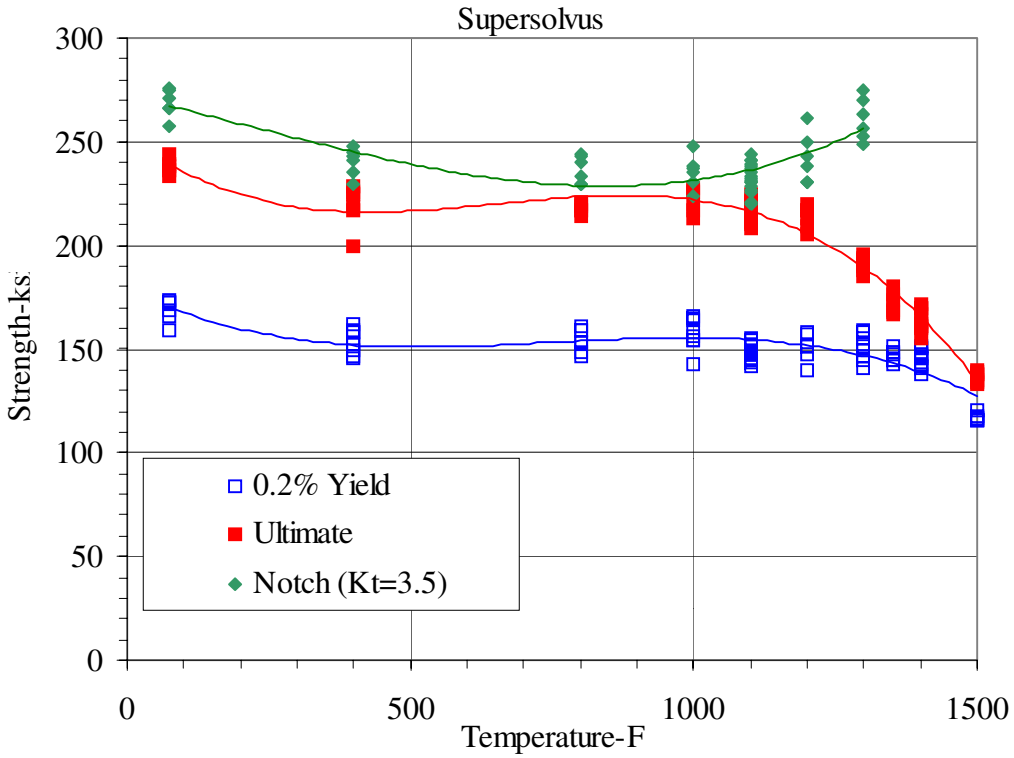

$YS = -0.0000000856T^3 + 0.0001925928T^2 - 0.1303862217T + 178.8337787200$

$R^2 = 0.6749797240$

$UTS = -0.0000001783T^3 + 0.0003492933T^2 - 0.2011345302T + 252.2139806884$

$R^2 = 0.9582802949$

$NTS = 0.0000000551T^3 - 0.0000320968T^2 - 0.0637384334T + 272.2389054116$

$R^2 = 0.6480397162$

Fig. 6. Comparisons of yield strength, ultimate tensile strength, and notch strength from supersolvus heat treated scaled-up disks.

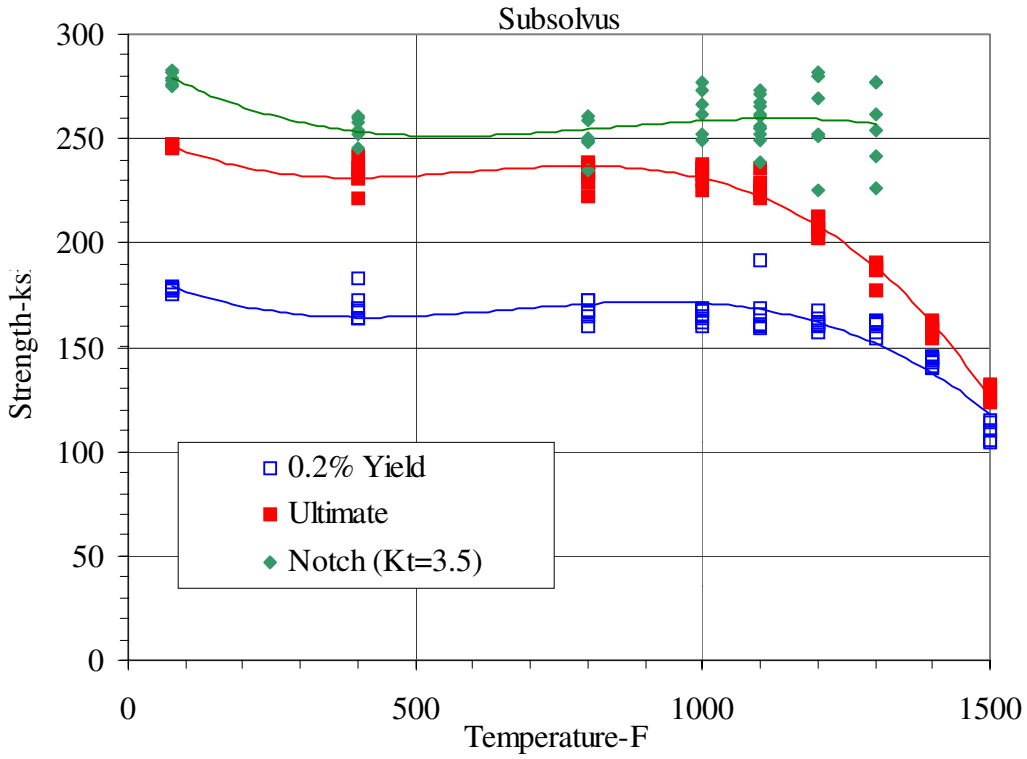

$YS = -0.0000001189T^3 + 0.0002375190T^2 - 0.1357683301T + 188.2550521542$

$R^2 = 0.8599851979$

$UTS = -0.0000001692T^3 + 0.0003003117T^2 - 0.1570735909T + 256.9533768296$

$R^2 = 0.9822889108$

$NTS = -0.0000000898T^3 + 0.0002274634T^2 - 0.1699066449T + 290.7420251533$

$R^2 = 0.2826300275$

Fig. 7. Comparisons of yield strength, ultimate tensile strength, and notch strength from subsolvus heat treated scaled-up disks.

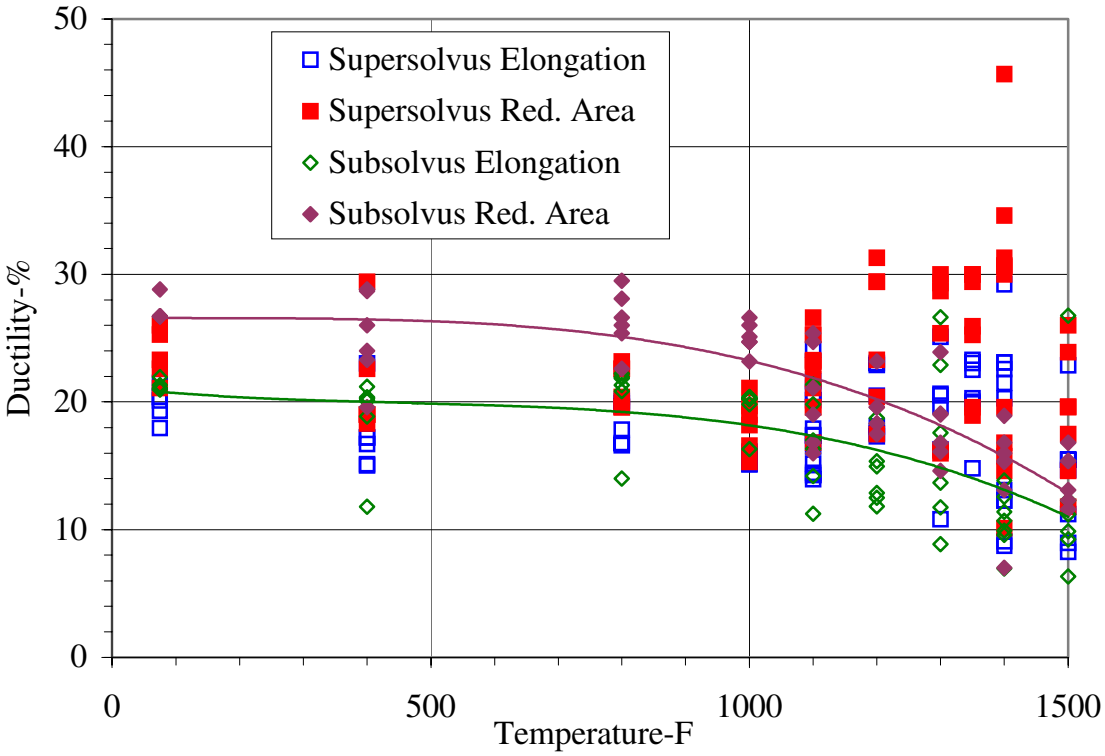

$SubRedArea = -0.0000000059T^3 + 0.0000032663T^2 - 0.0007123647T + 26.6121493052$

$R^2 = 0.7184447841$

$SubElong = -0.0000000067T^3 + 0.0000092076T^2 - 0.0054917597T + 21.1611870207$

$R^2 = 0.3656757096$

Fig. 8. Comparisons of elongation and reduction in area from supersolvus and subsolvus heat treated scaled-up disks; supersolvus mean elongation and mean reduction in area did not significantly vary with temperature.

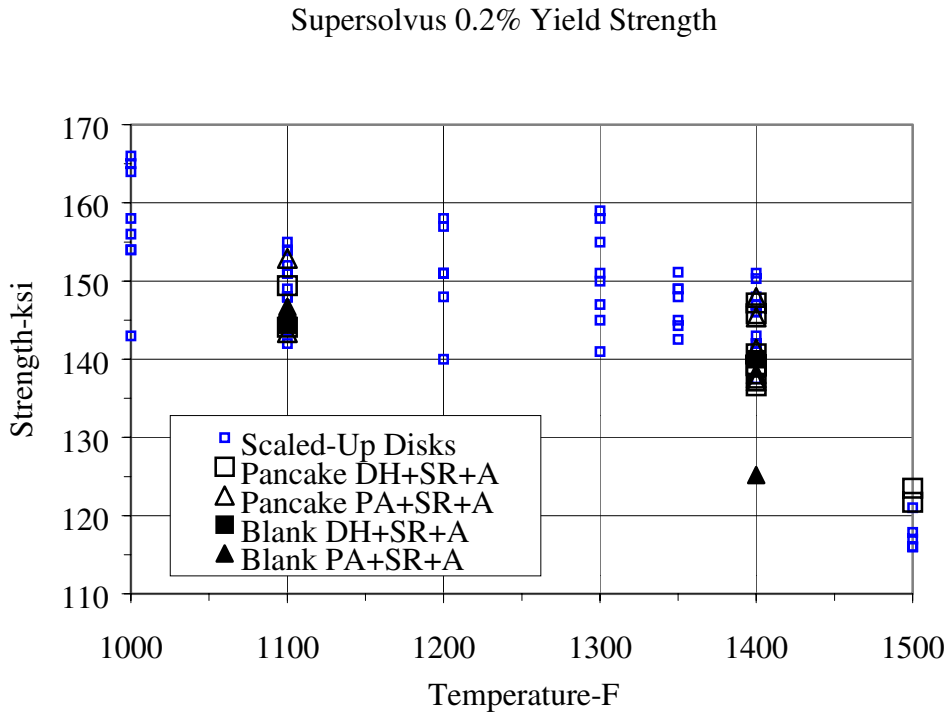

a.

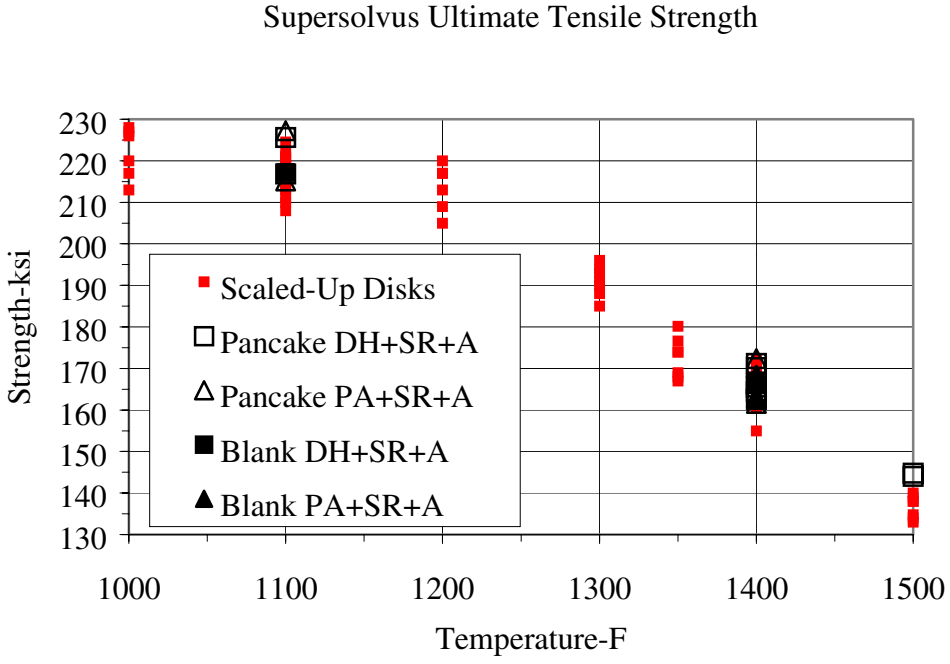

b.

Fig. 9. Comparison of scaled-up and subscale tensile a) yield strengths, and b) ultimate strengths with solution heat treat variations pre-annealed (PA) and direct heatup (DH), with comparable stress relief and aging heat treatments.

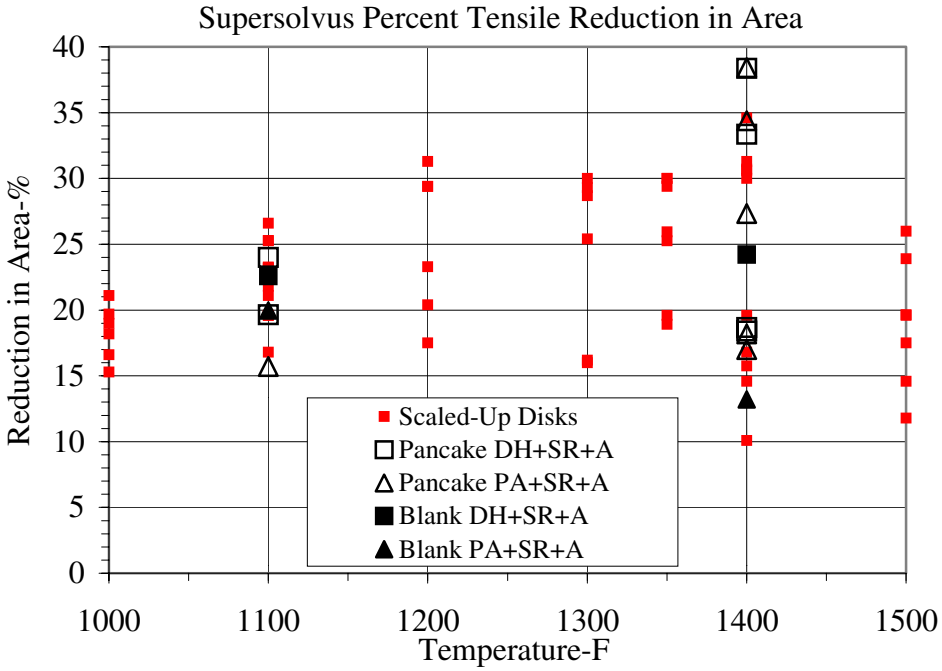

Fig. 10. Comparison of scaled-up and subscale reductions in area with solution heat treat variations pre-annealed (PA) and direct heatup (DH), with comparable stress relief and aging heat treatments.

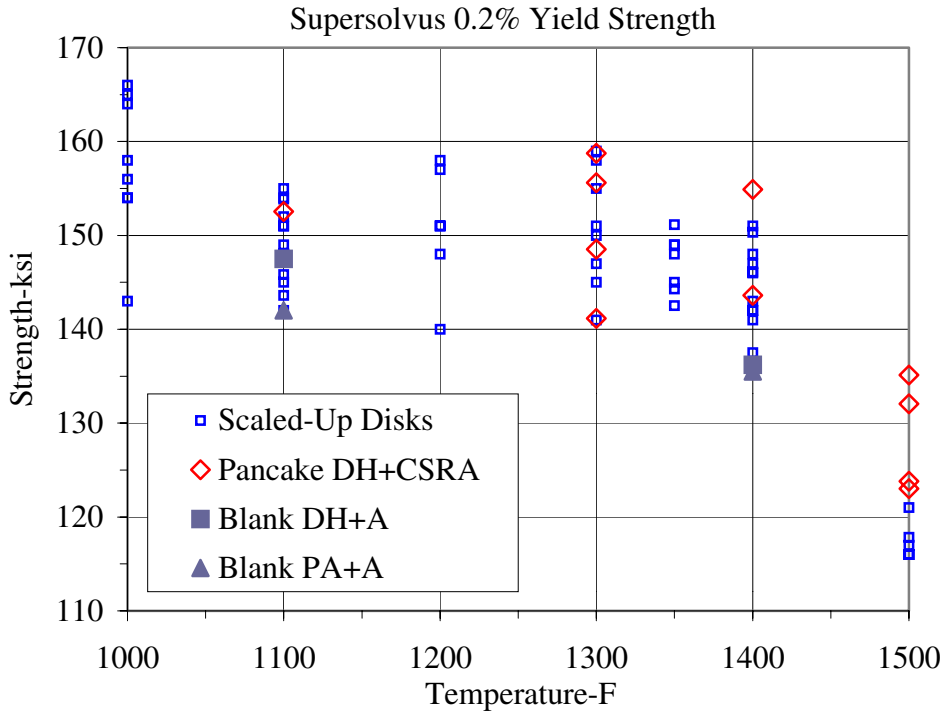

Fig. 11. Comparison of yield strengths, baseline scaled-up versus subscale disks with combined stress relief +aging heat treat, and blanks not given stress relief.

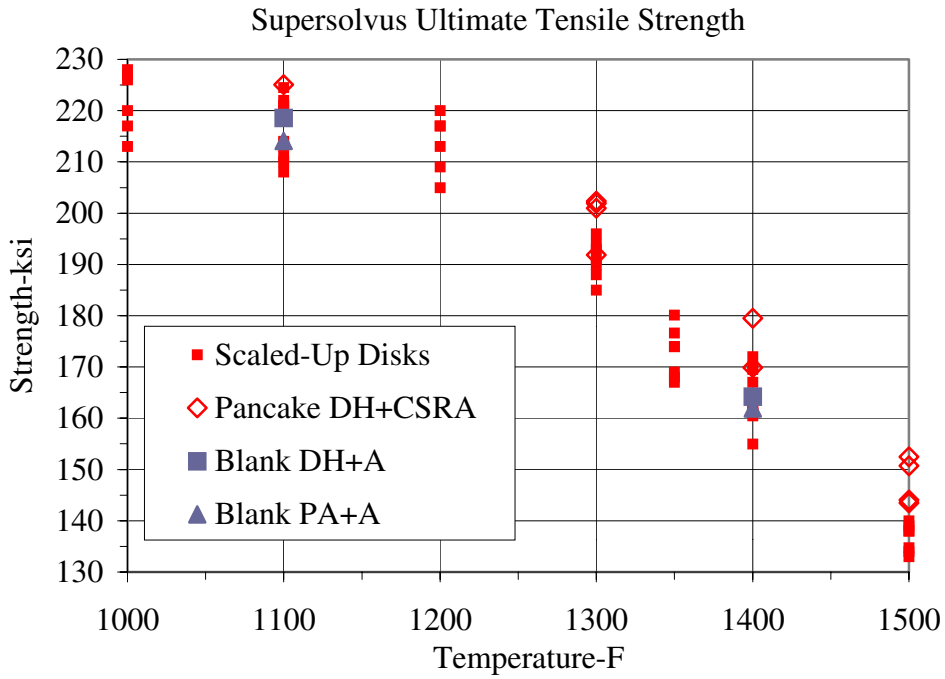

Fig. 12. Comparison of ultimate tensile strengths, baseline scaled-up versus subscale disks with combined stress relief +aging heat treat, and blanks not given stress relief.

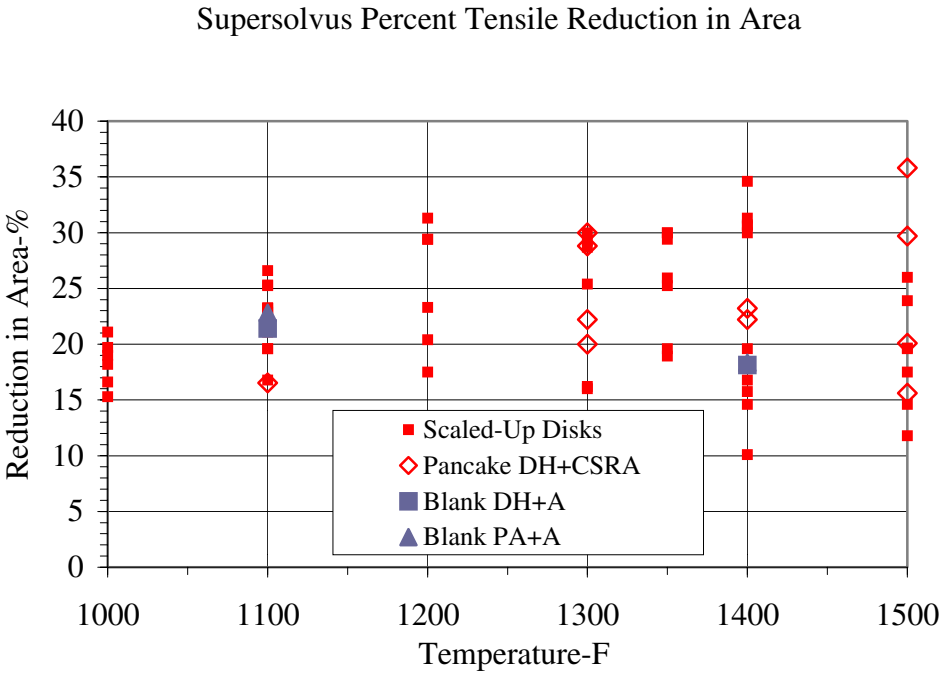

Fig. 13. Comparison of reductions in area, baseline scaled-up versus subscale disks with combined stress relief +aging heat treat, and blanks not given stress relief.

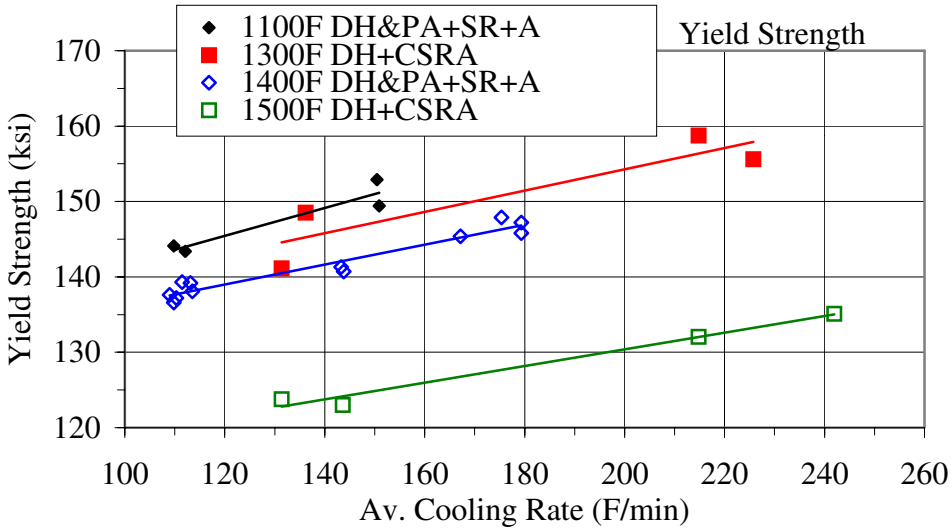

YS(1100F) = 0.185CR + 123.25
R^2 = 0.8846

YS(1300F) = 0.1415CR + 125.97
R^2 = 0.8186

YS(1400F) = 0.1323CR + 123.1
R^2 = 0.9408

YS(1500F) = 0.1106CR + 108.28
R^2 = 0.9793

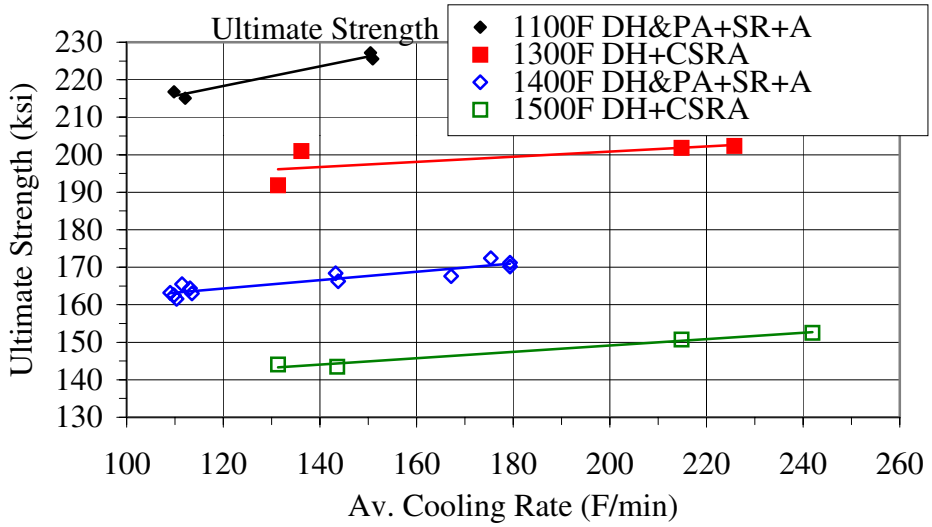

UTS(1100F)= 0.2611CR + 187.01
R^2 = 0.9631

UTS(1300F) = 0.0684CR + 187.14
R^2 = 0.479

UTS(1400F) = 0.1112CR + 151.02
R^2 = 0.8637

UTS(1500F) = 0.0844CR + 132.26
R^2 = 0.976

Fig. 14. Effect of cooling rate on yield and ultimate strengths of subscale disks.

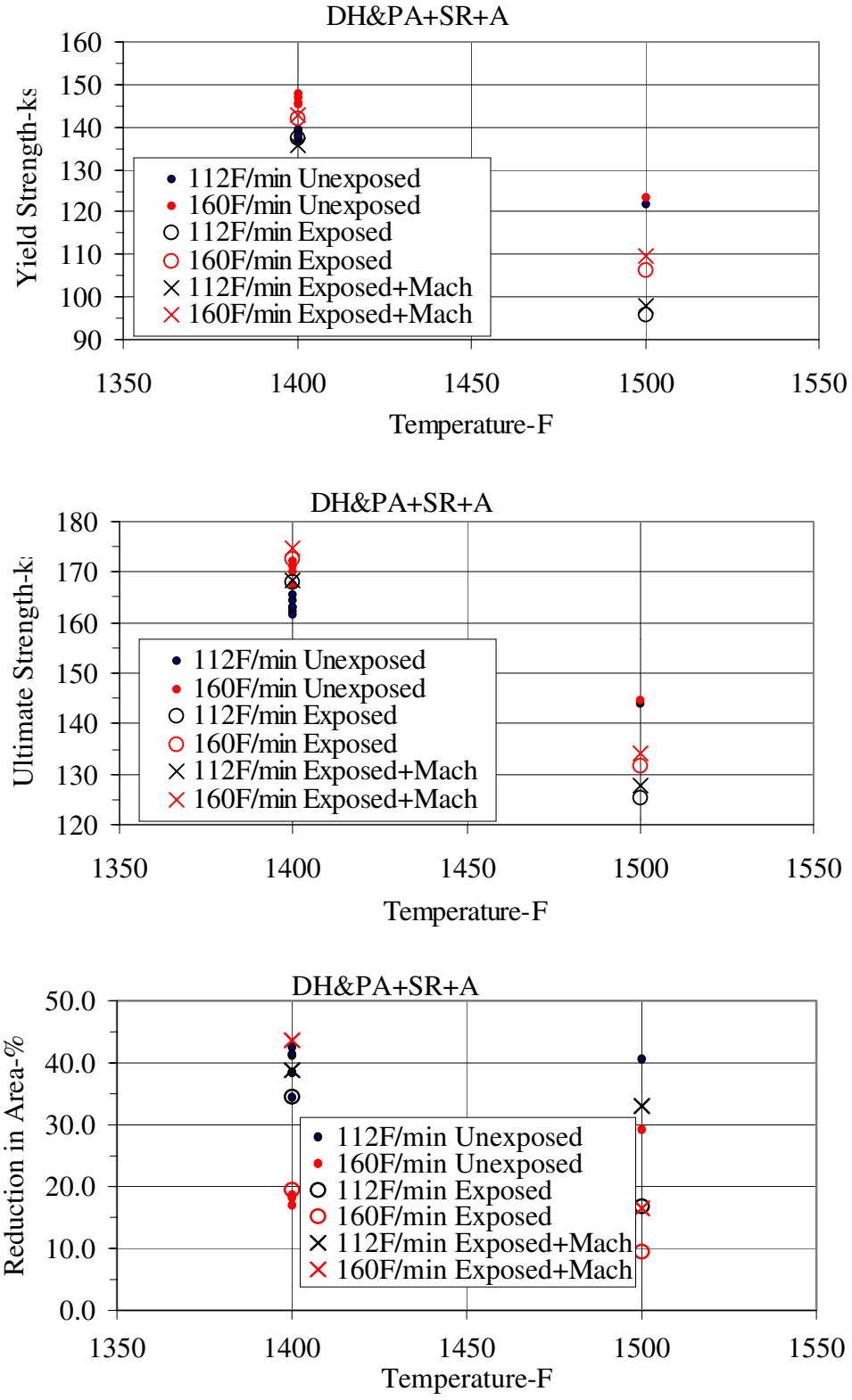

Fig. 15. Effects of exposures on strengths and ductilities of subscale disks.

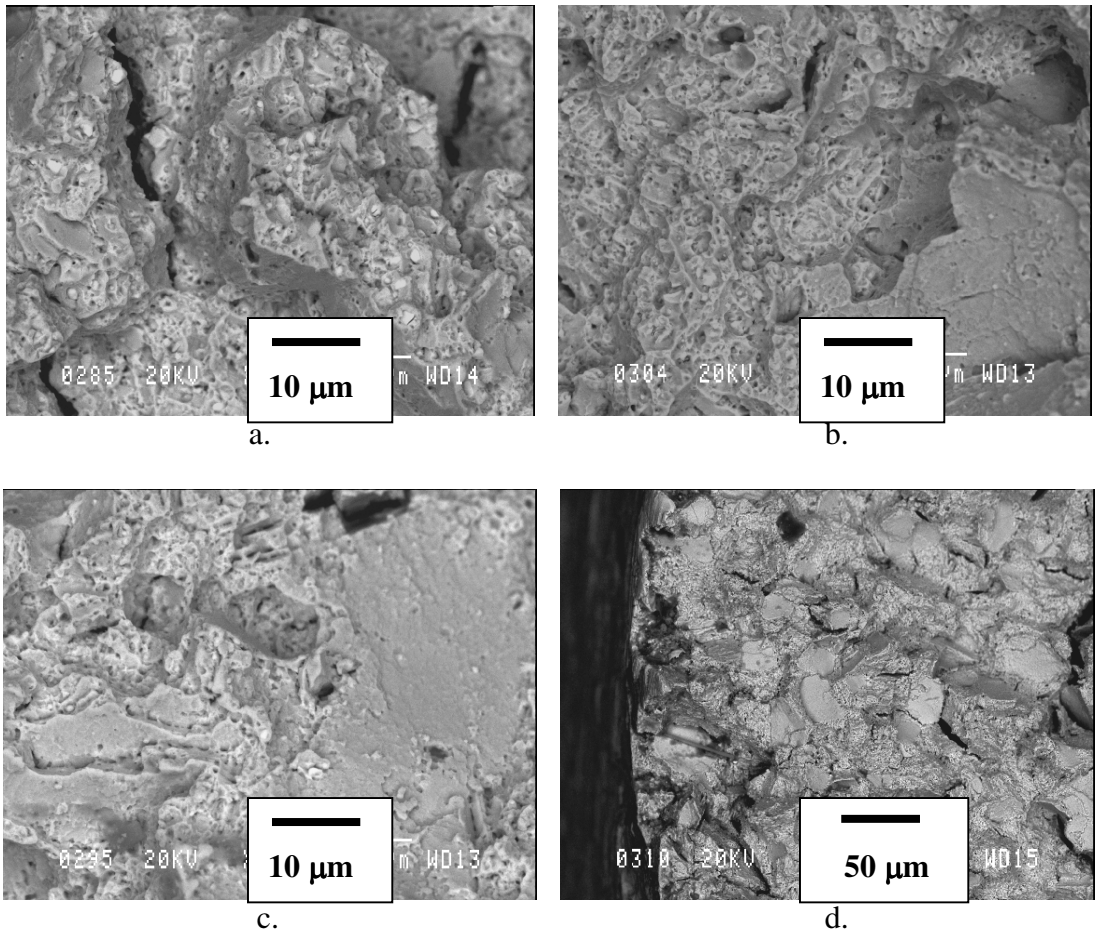

Fig. 16. Tensile failure modes at: a) 75 °F: microvoid coalescence, b) 800 °F: microvoid coalescence plus grain slip failures, c) 1200 °F: microvoid coalescence plus grain slip failures, d) 1500 °F: intergranular surface cracking plus internal microvoid coalescence.

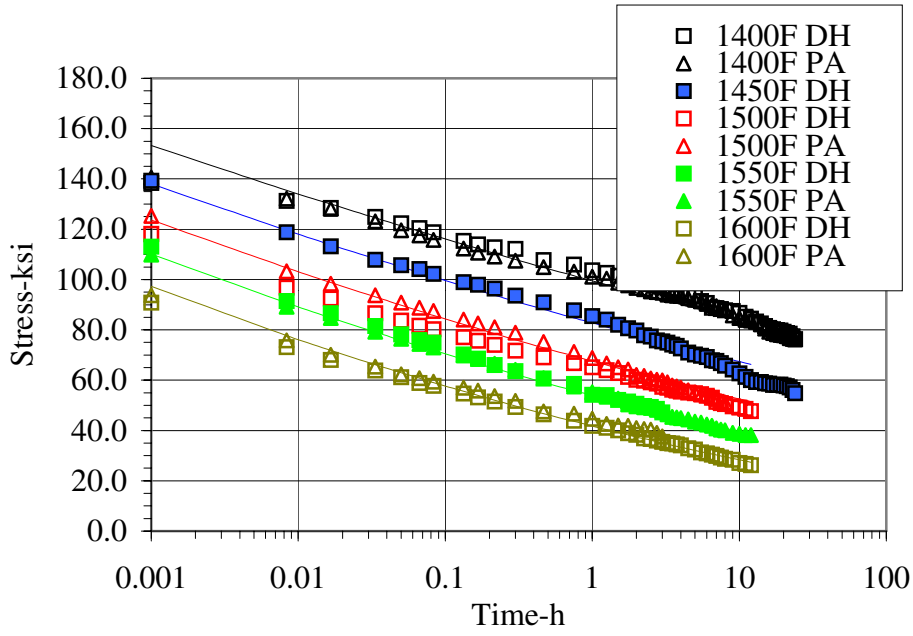

$$\sigma = (88.618925+8.895715*\log(t)-0.082203T-0.007791*\log(t)*T)^2$$

$$R^2=0.9838$$

Fig. 17. Comparison of stress relaxation versus time (t) and temperature (T) in tests of specimens after PA and DH solution heat treatments.

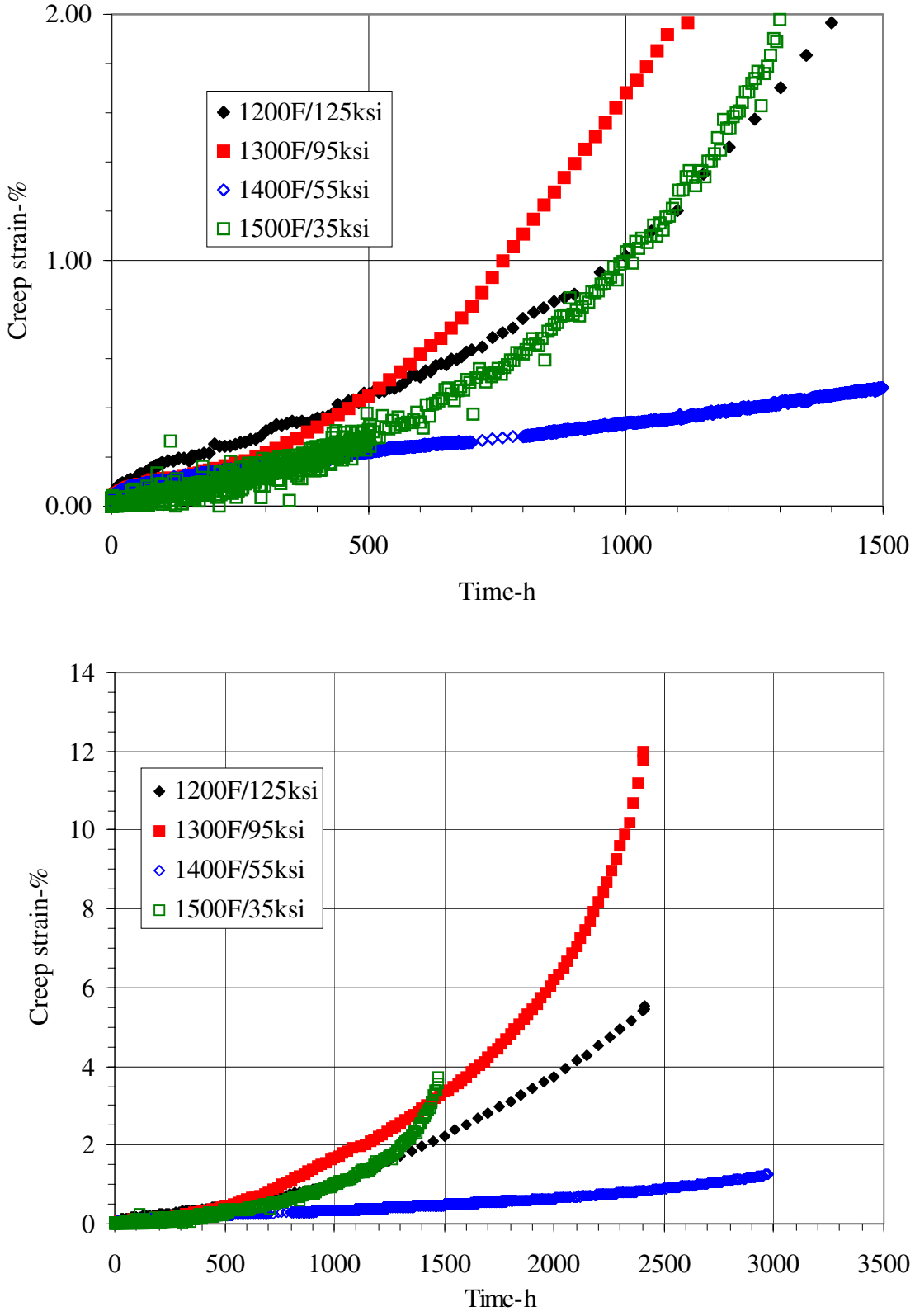

Fig. 18. Typical creep curves, tests run to rupture.

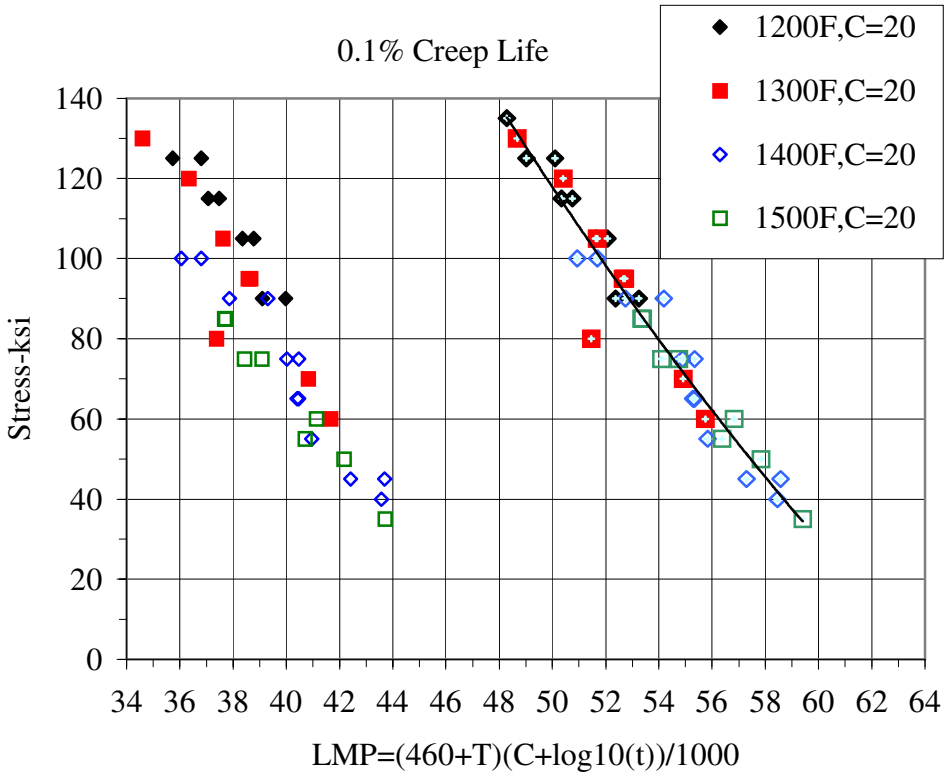

$$\sigma = 0.1195LMP^2 - 21.95LMP + 916.42$$

$$C=28,\ R^2 = 0.9489$$

Fig. 19. Larson-Miller parameter versus stress for time to 0.1% creep, using Larson-Miller constants (C) of 20 and 28.

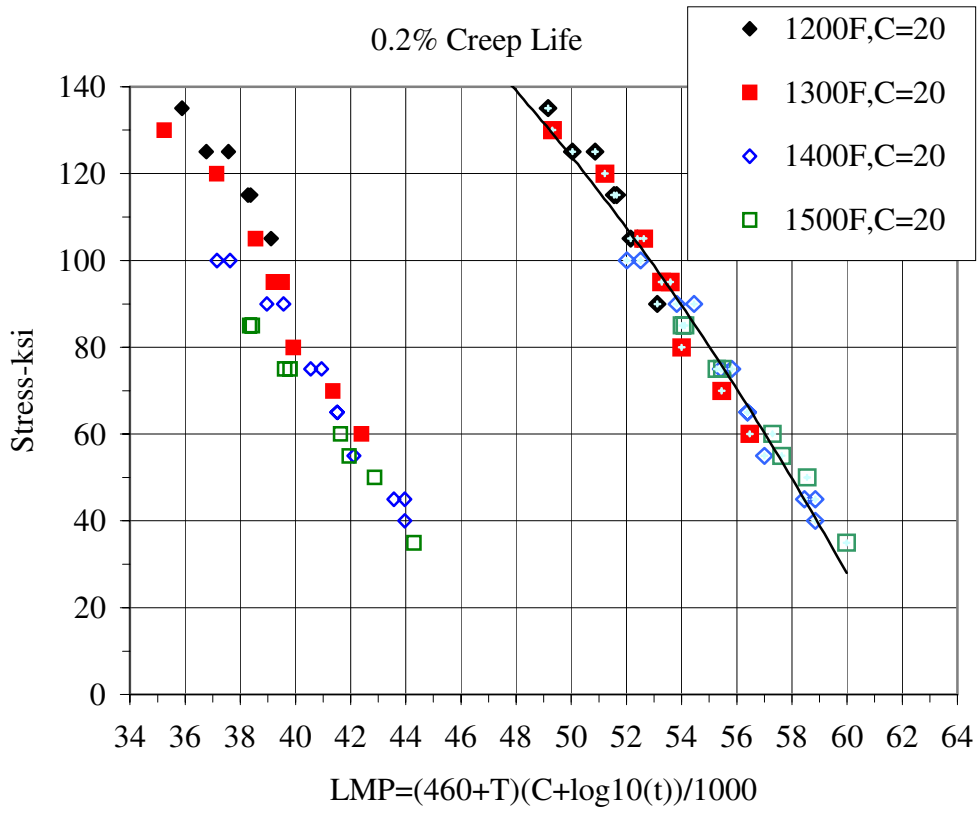

$$\sigma = -0.1715LMP^2 + 9.2468LMP + 90.233$$

$$C=28,\ R^2 = 0.9745$$

Fig. 20. Larson-Miller parameter versus stress for time to 0.2% creep, using Larson-Miller constants (C) of 20 and 28.

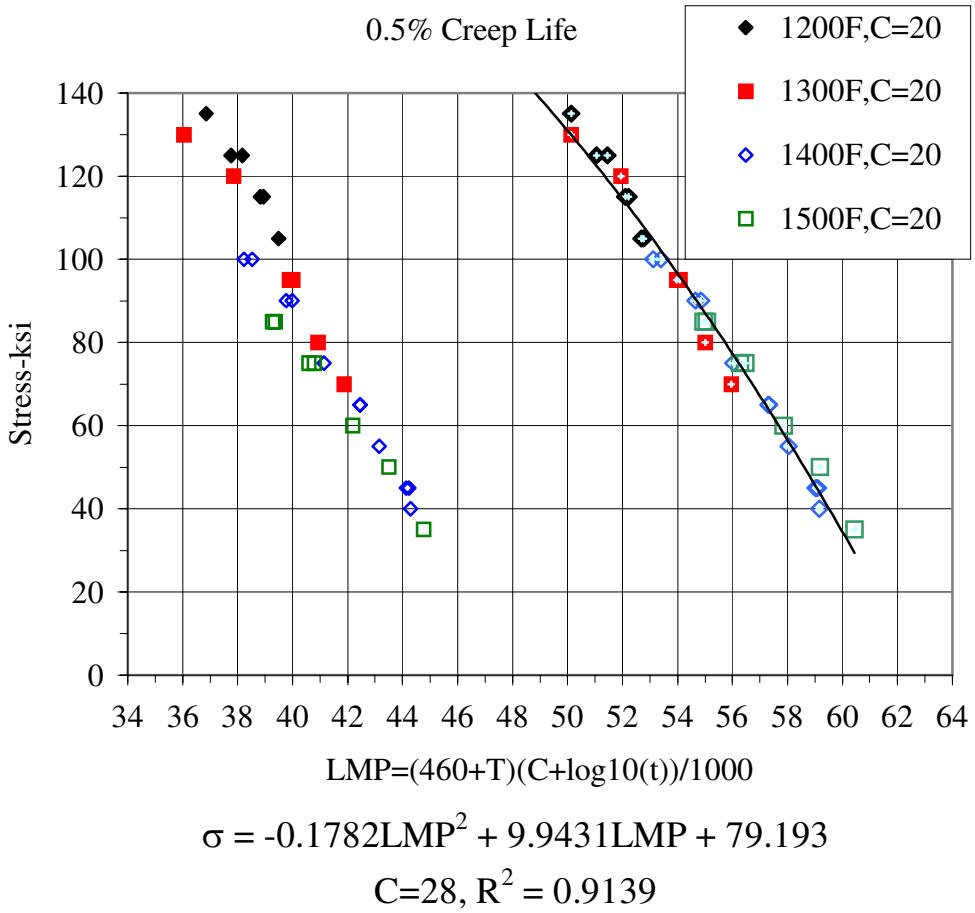

Fig. 21. Larson-Miller parameter versus stress for time to 0.5% creep, using Larson-Miller constants (C) of 20 and 28.

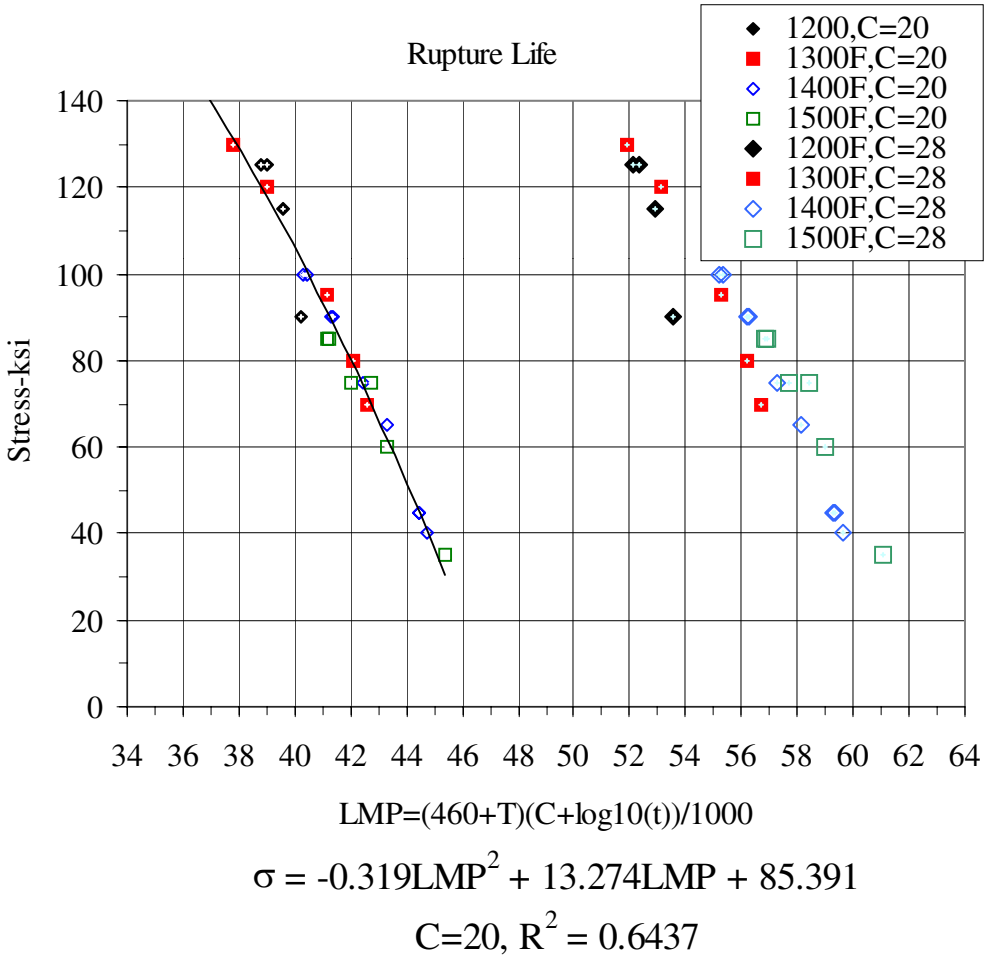

Fig. 22. Larson-Miller parameter versus stress for time to rupture, using Larson-Miller constants (C) of 20 and 28.

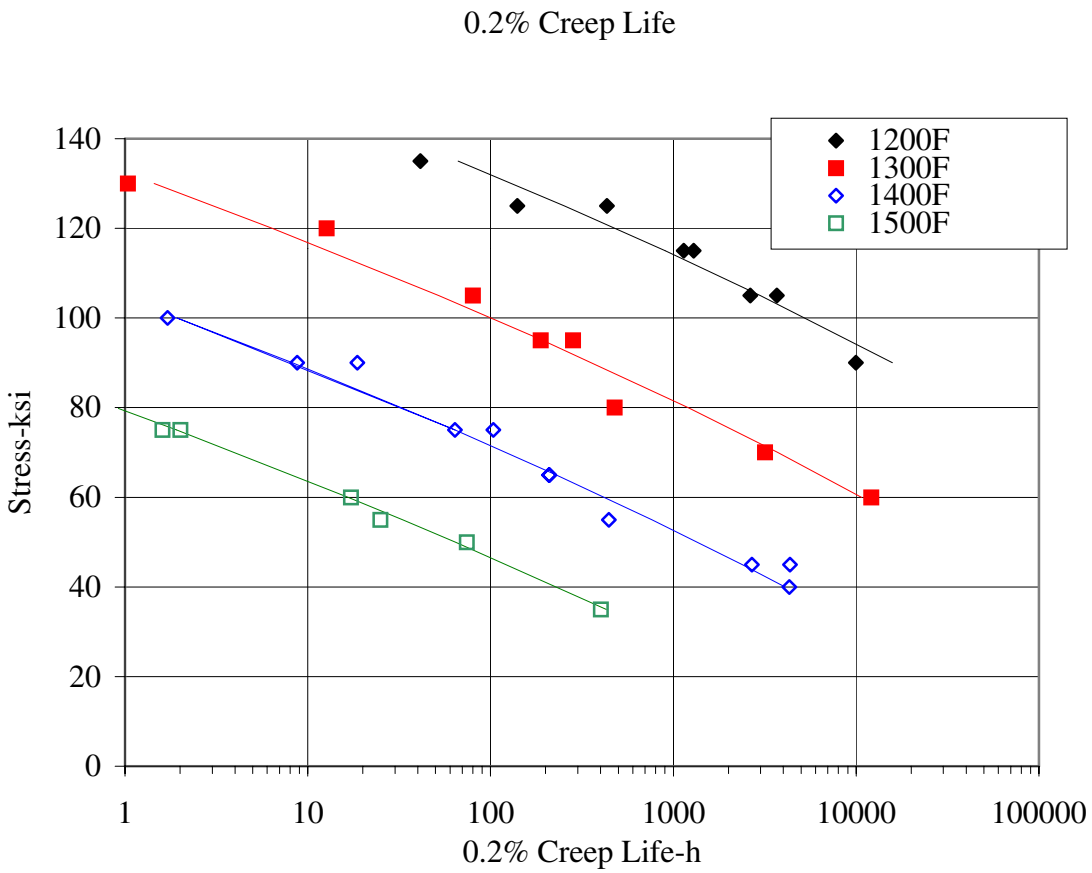

$$\log(0.2\%\ \text{life}) = 18.230123 + 0.076886\sigma - 0.009298T - 0.000079\sigma T - 0.000155\sigma^2$$
$$R^2 = 0.9829$$

Fig. 23. Time to 0.2% creep versus stress using multiple quadratic regression.

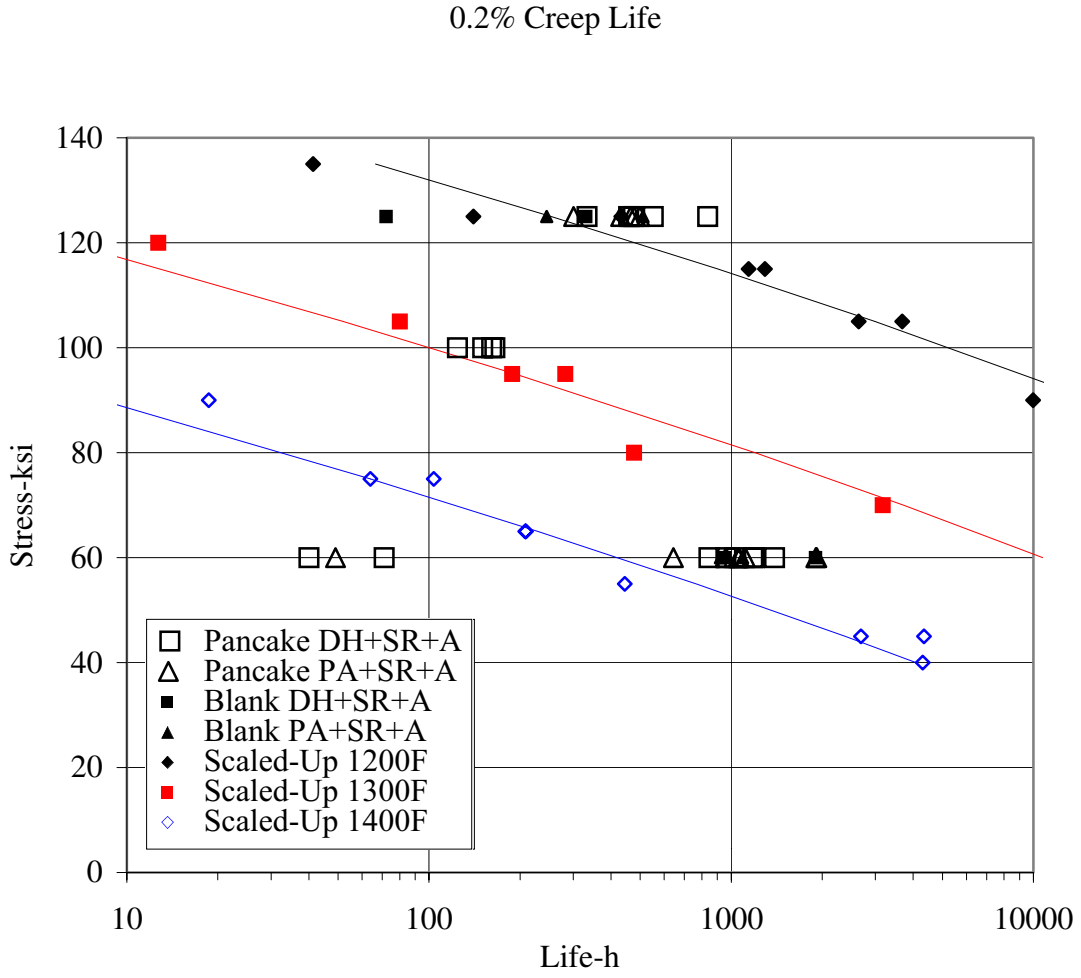

Fig. 24. Comparison of time to 0.2% creep for baseline scaled-up case versus subscale disks and blanks having solution heat treat variations pre-annealed (PA) and direct heatup (DH), using comparable stress relief and aging heat treatments.

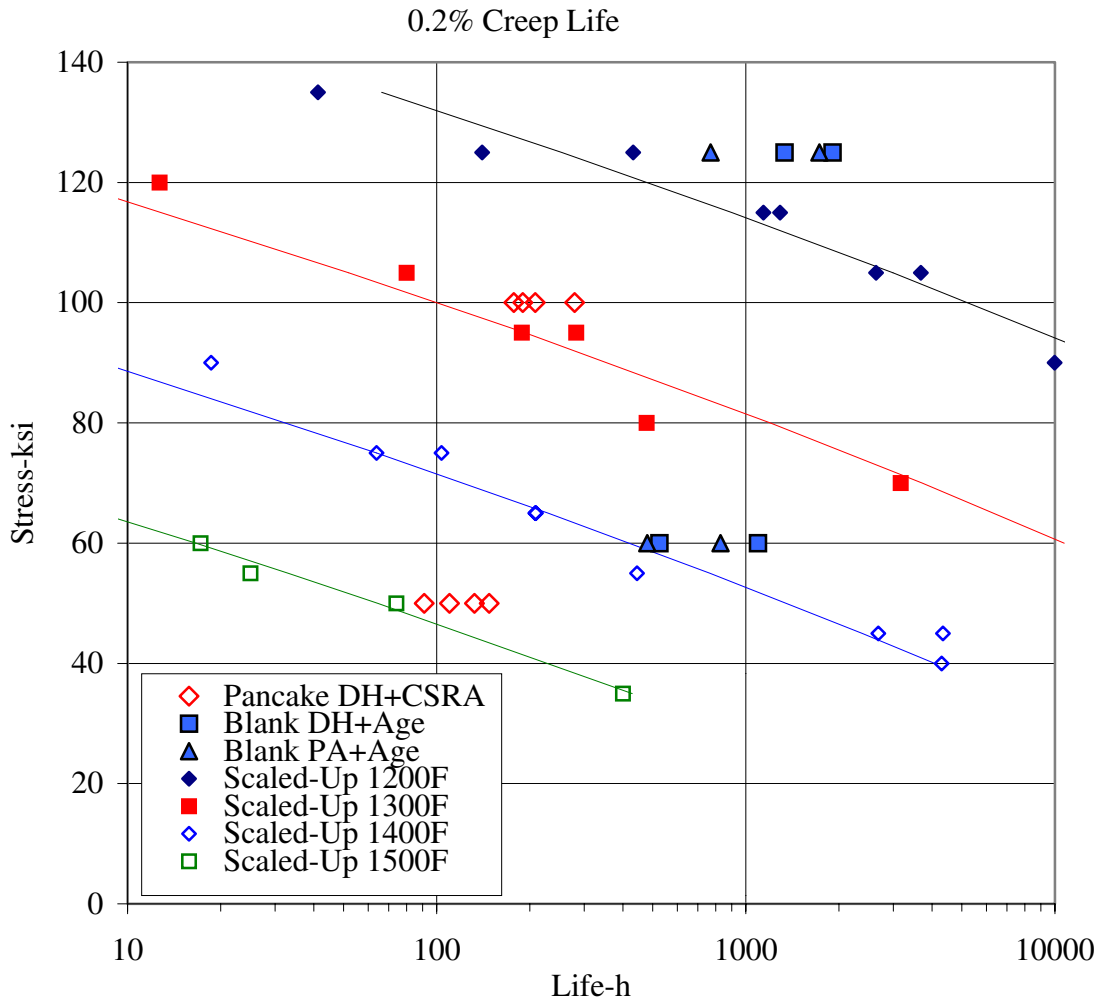

Fig. 25. Comparison of time to 0.2% creep for baseline scaled-up case versus subscale disks with combined stress relief +aging heat treatment, and blanks with stress relief removed.

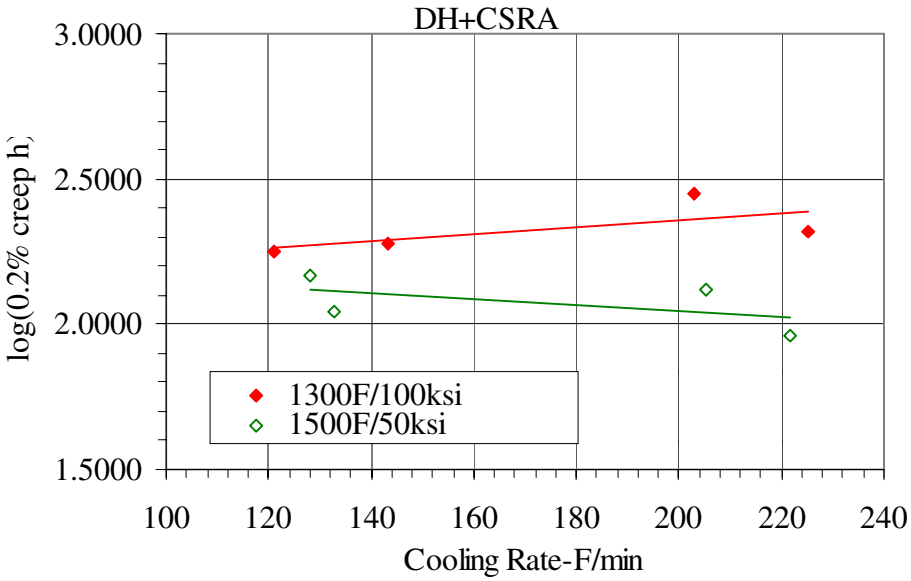

Fig. 26. Effect of cooling rate on creep resistance in DH+CSRA subscale disks.

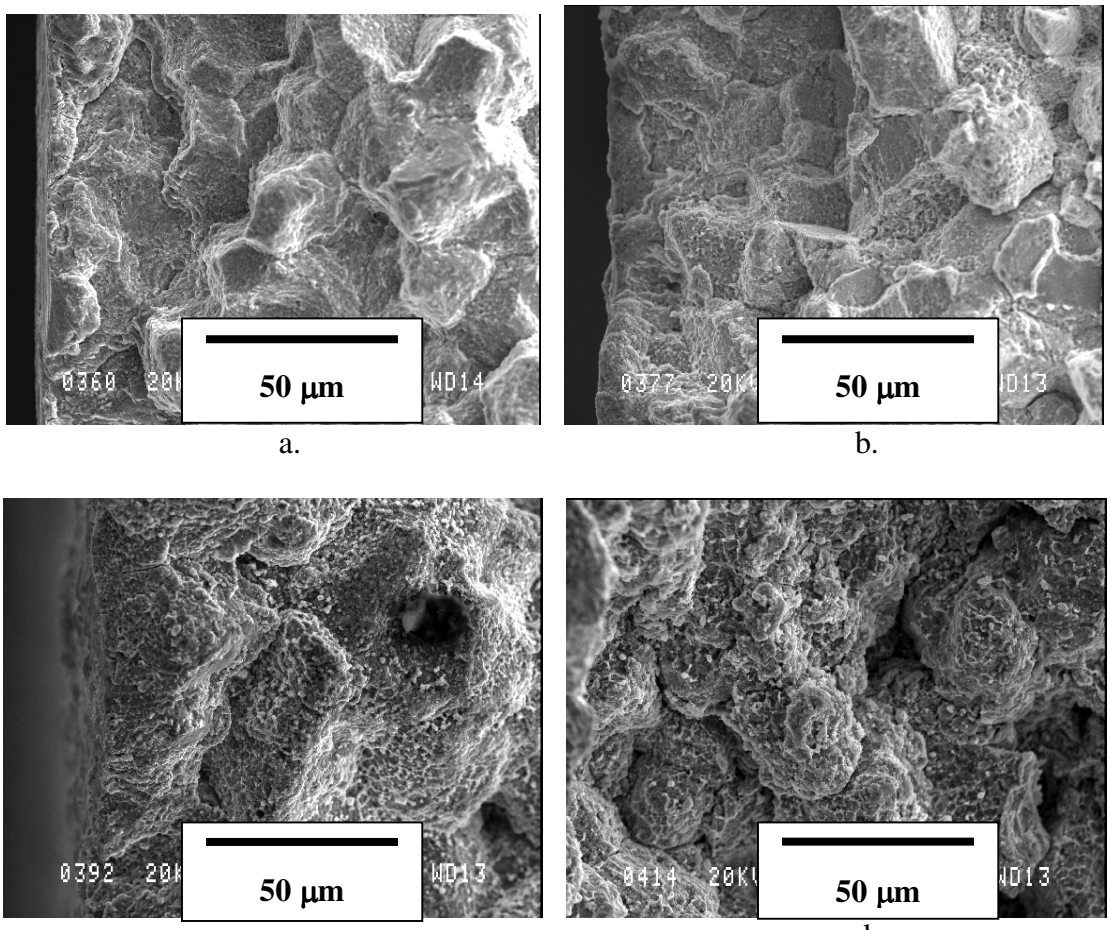

a. b.

c. d.

Fig. 27. The typical creep failure modes of intergranular surface cracking:
a) 1200 °F/115 ksi/7090.1h; b) 1300 °F/95 ksi/2400.1h; c) 1400 °F/45 ksi/7695.1h;
d) 1500 °F/30ksi/1829h.

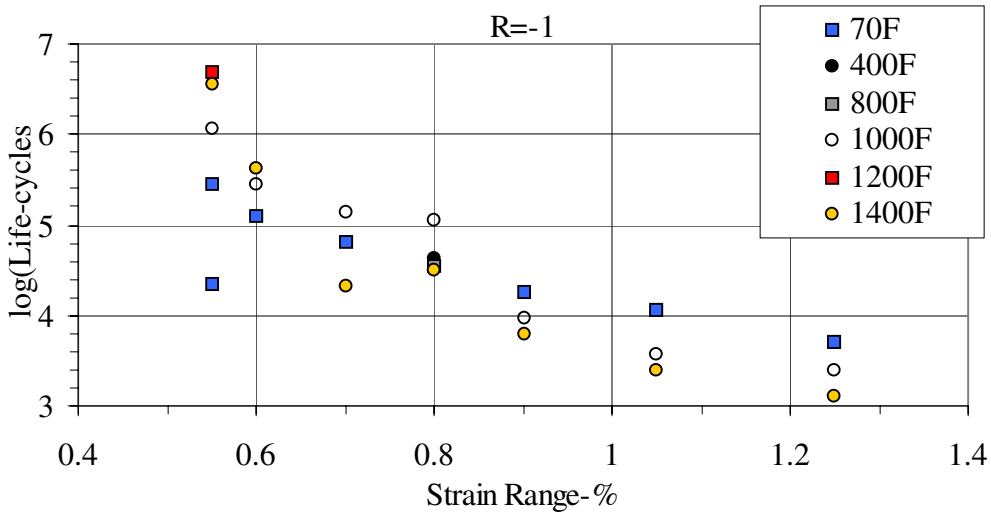

a.

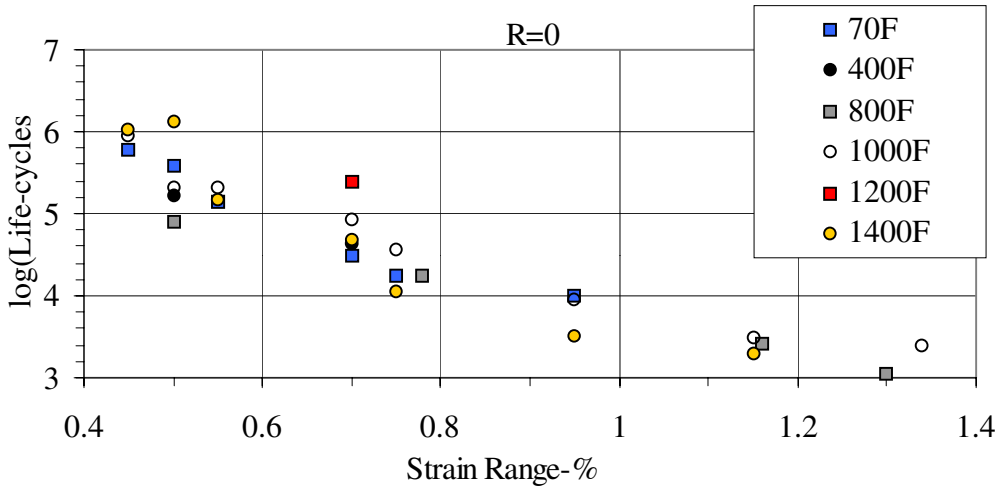

b.

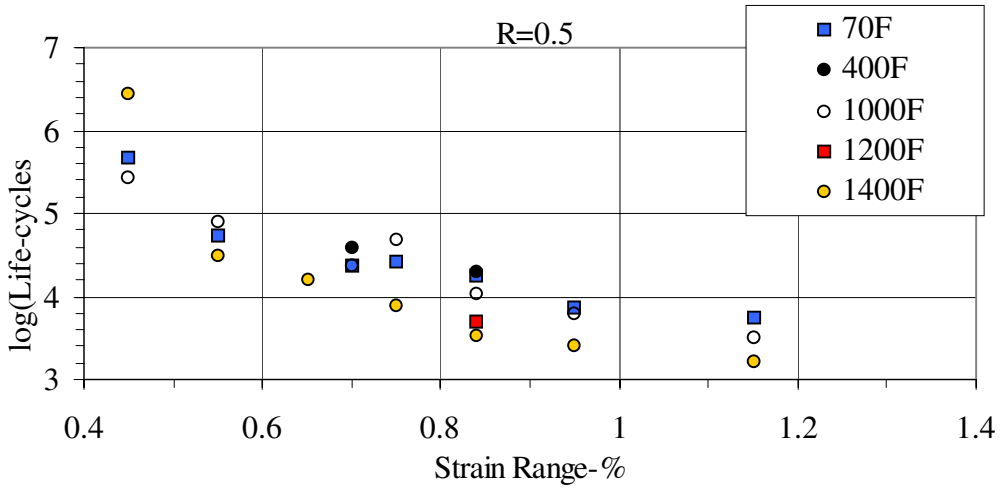

c.

Fig. 28. Low cycle fatigue life versus strain range at a) R_ε=-1, b) R_ε=0, c) R_ε=0.5.

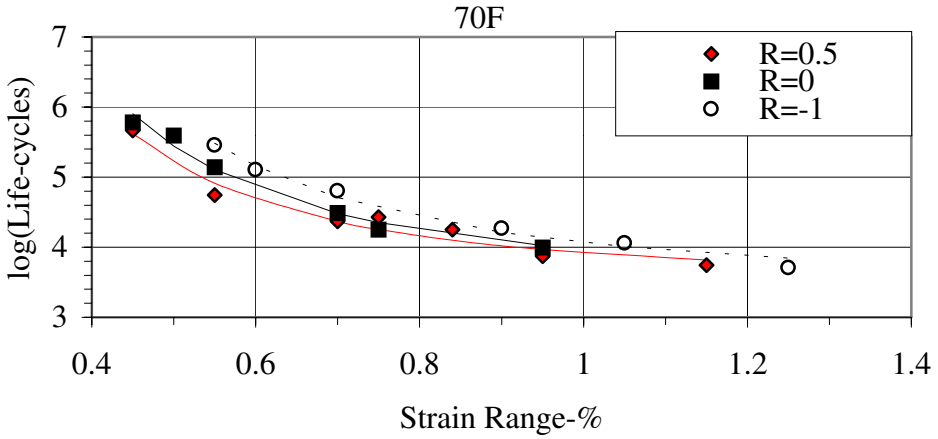

a. 70 °F: $\log(life)=3.477516+0.013860(1/\Delta\varepsilon)^2+0.026668R_\varepsilon-0.000012(1/\Delta\varepsilon)^2R_\varepsilon$
$R^2=0.9727$

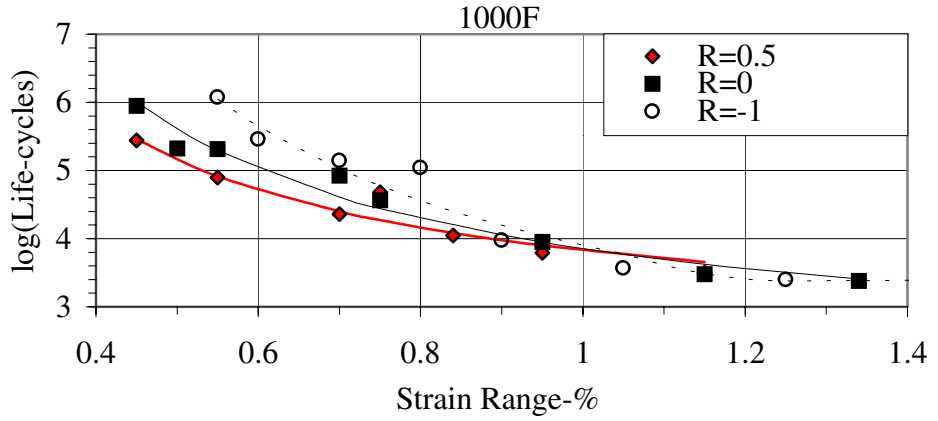

b. 1000 °F: $\log(life)=2.096100+0.017591(1/\Delta\varepsilon)+0.811451R_\varepsilon-0.008613(1/\Delta\varepsilon)R_\varepsilon$
$R^2=0.9475$

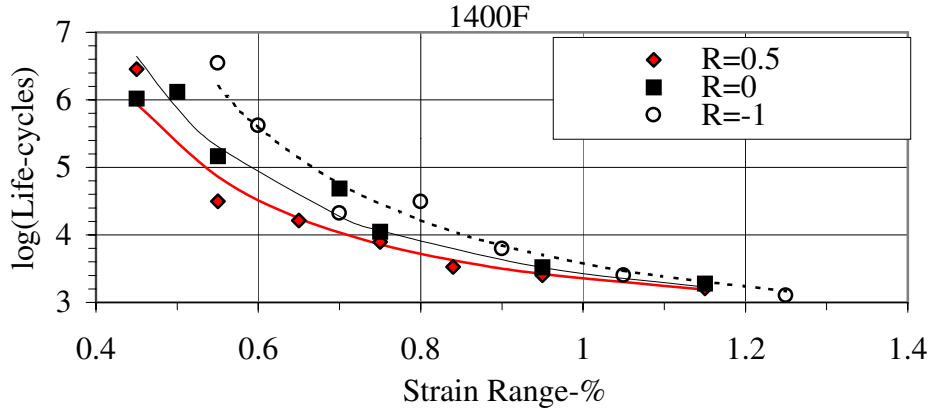

c. 1400 °F: $\log(life)=2.609246+0.0000817(1/\Delta\varepsilon)^2+0.1696561R_\varepsilon-0.000032\,(1/\Delta\varepsilon)^2\,R_\varepsilon$
$R^2=0.9420$

Fig. 29. Fatigue life regressions at a) 70, b) 1000, and c) 1400 °F.

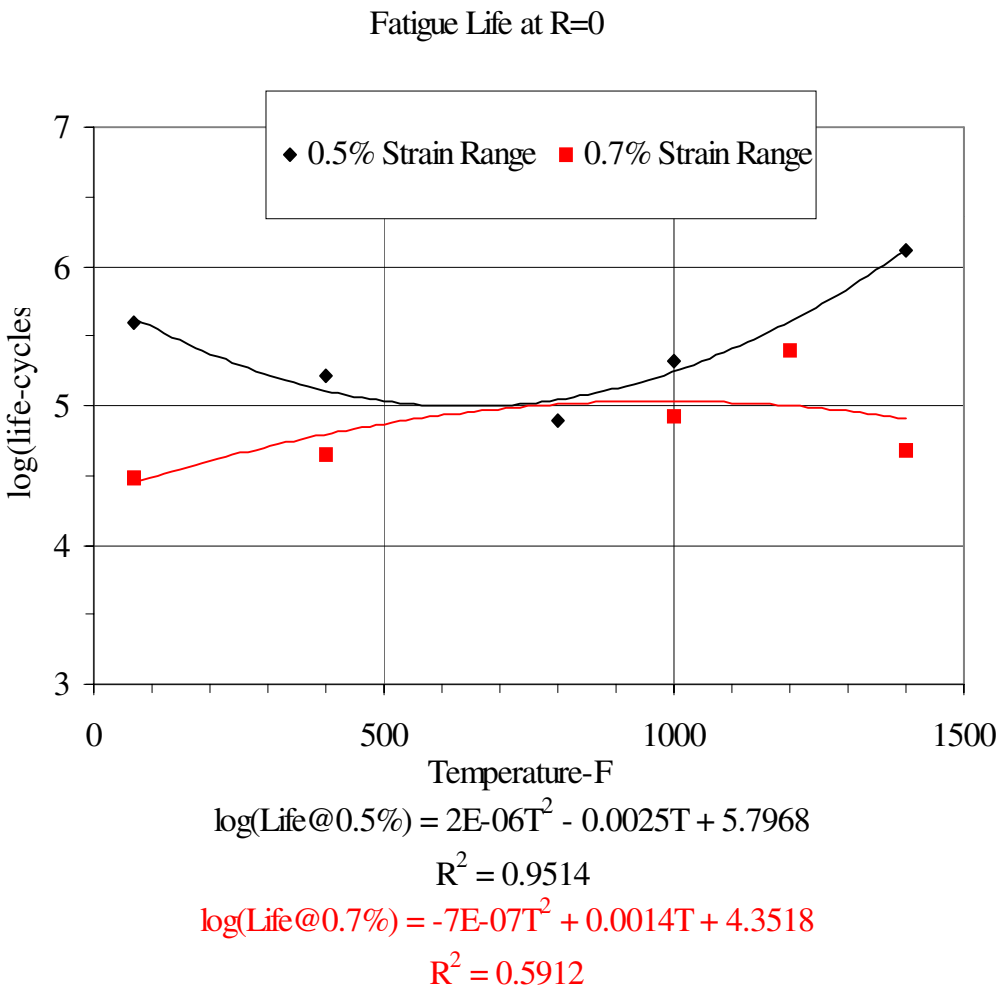

Fig. 30. Simplified fatigue life versus temperature relationships at strain ratio of 0.

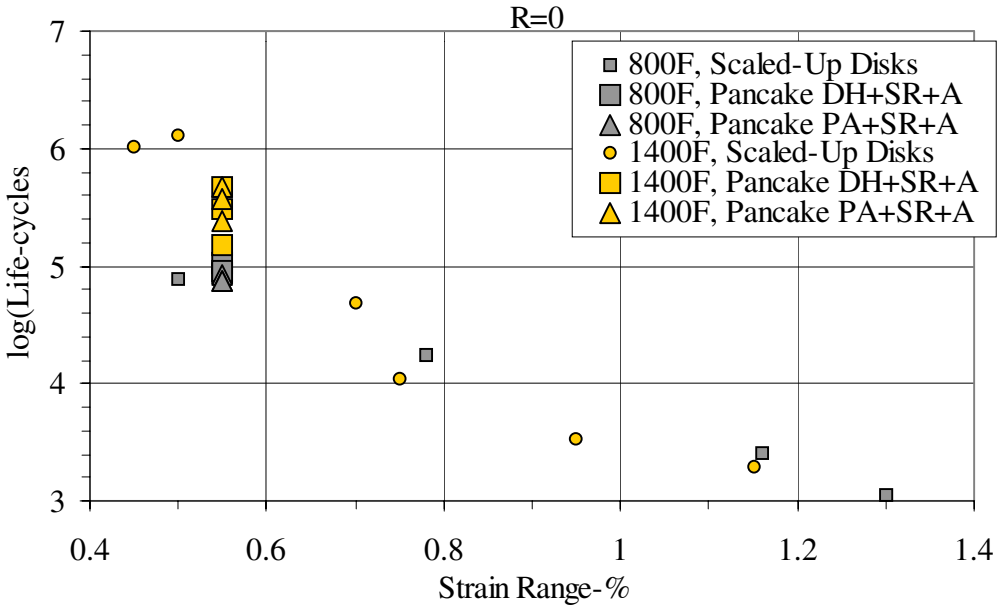

Fig. 31. Comparison of strain range-life responses for scaled-up and pancake material

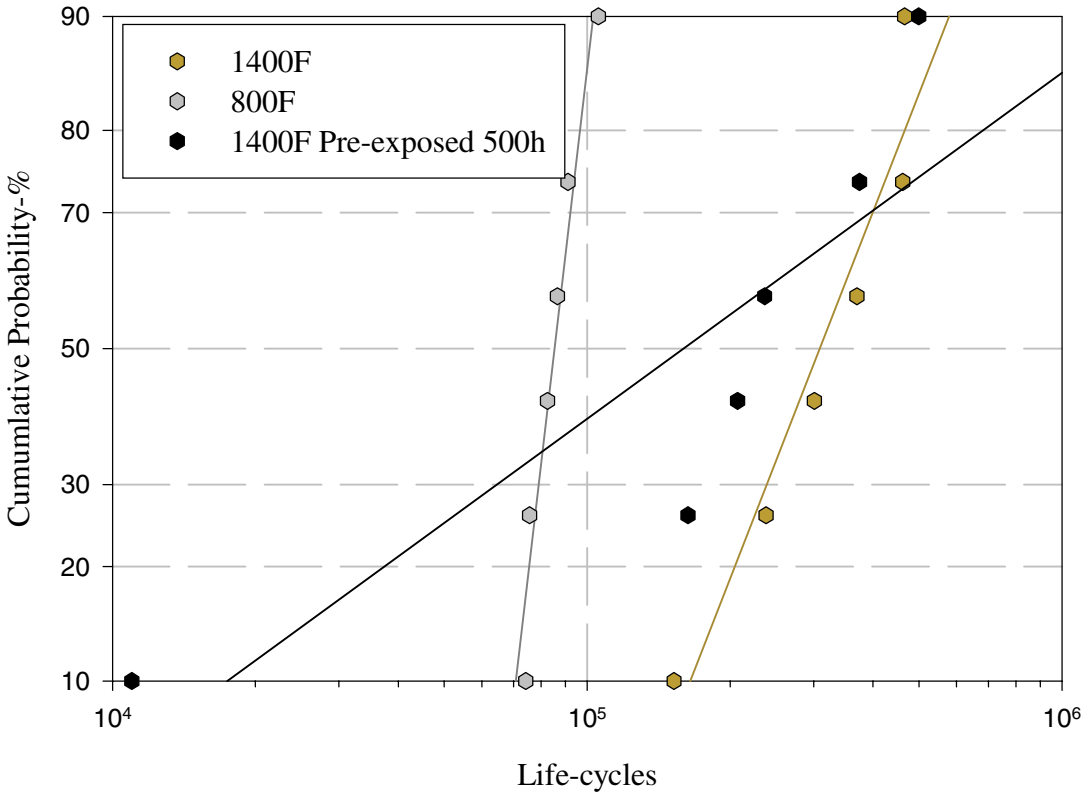

Fig. 32. Probability plot comparing life of subscale disk specimens at 800 and 1400 °F, and prior-exposure effects.

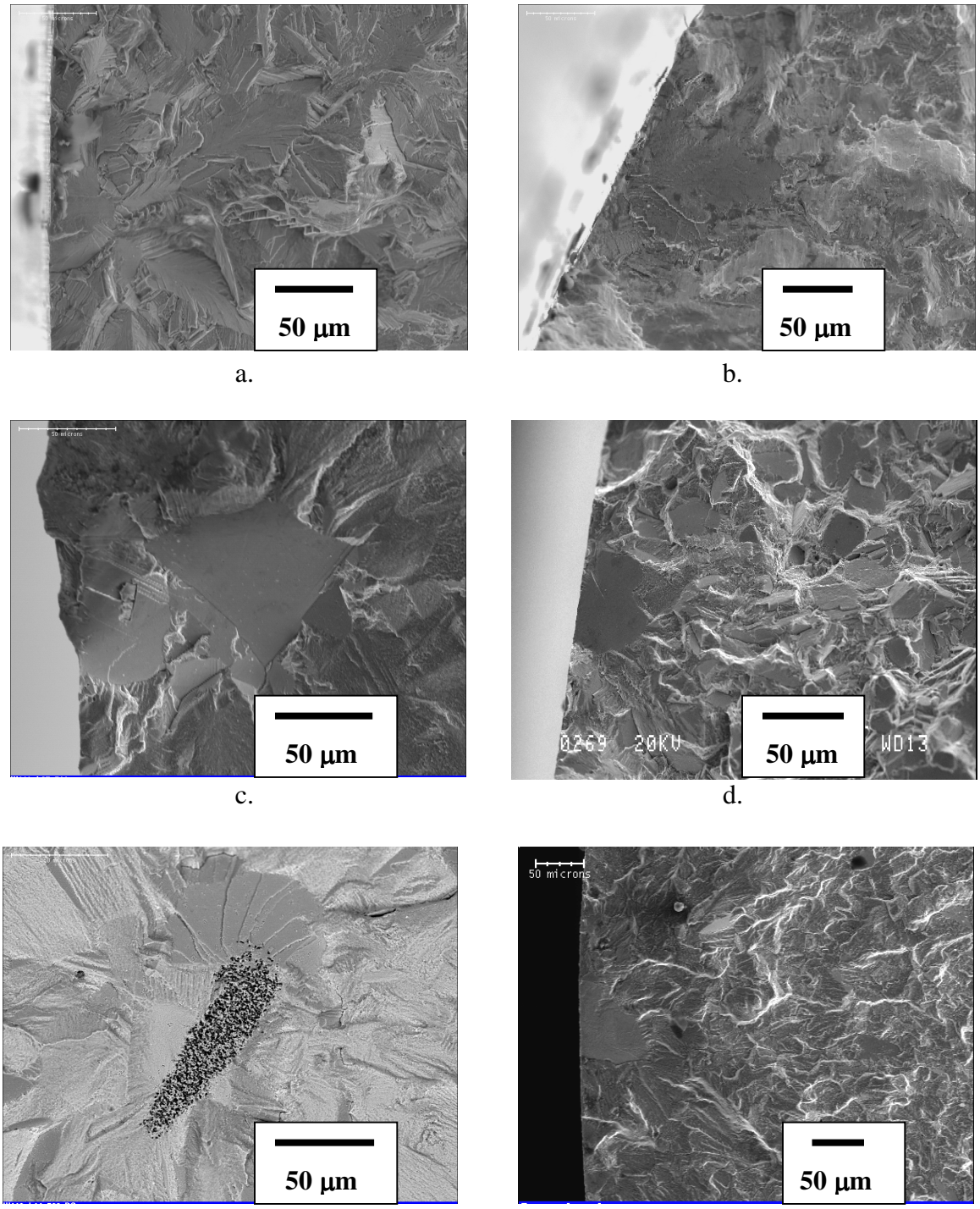

Fig. 33. Failure initiation points in LCF specimens tested at R_ε=0: a) 75 °F, Δε=0.5%: surface grain facet; b) 75 °F, Δε=1.15%: multiple surface grain facets; c) 800 °F, Δε=0.5%: surface grain facet; d) 800 °F, Δε=1.15%: multiple surface grain facets; e) 1400 °F, Δε=0.45%: internal ceramic inclusion; f) 1400 °F, Δε=1.15%: multiple surface grain facets.

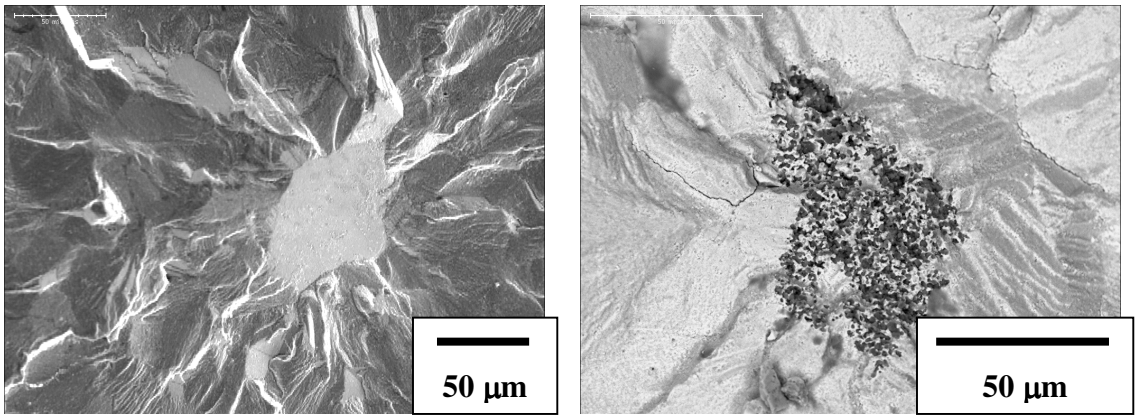

a. b.

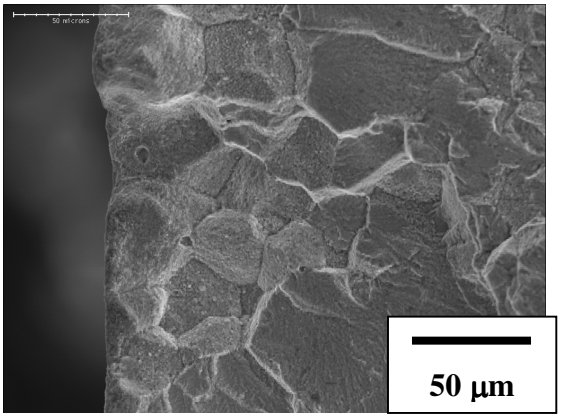

c.

Fig. 34. Failure initiation points of specimens LCF tested at 1400 °F, $\Delta\varepsilon$=0.7%, R_ε=0 after 1400 °F/500h exposure: a. single internal grain facet, life = 499,289 cycles; b. single internal Type 2 alumina-rich inclusion, life = 162,977 cycles; c. single surface intergranular crack, life = 10,994 cycles.

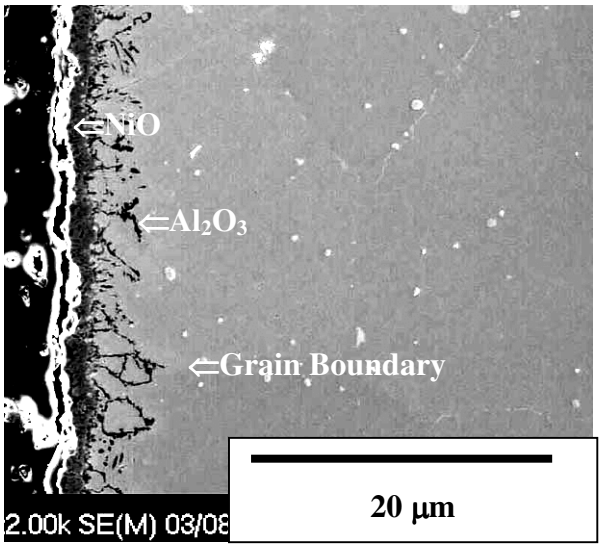

Fig. 35. Typical oxidized surface of 1400 °F/500h exposed LCF specimens, with outer NiO layer and inner branches of Al_2O_3.

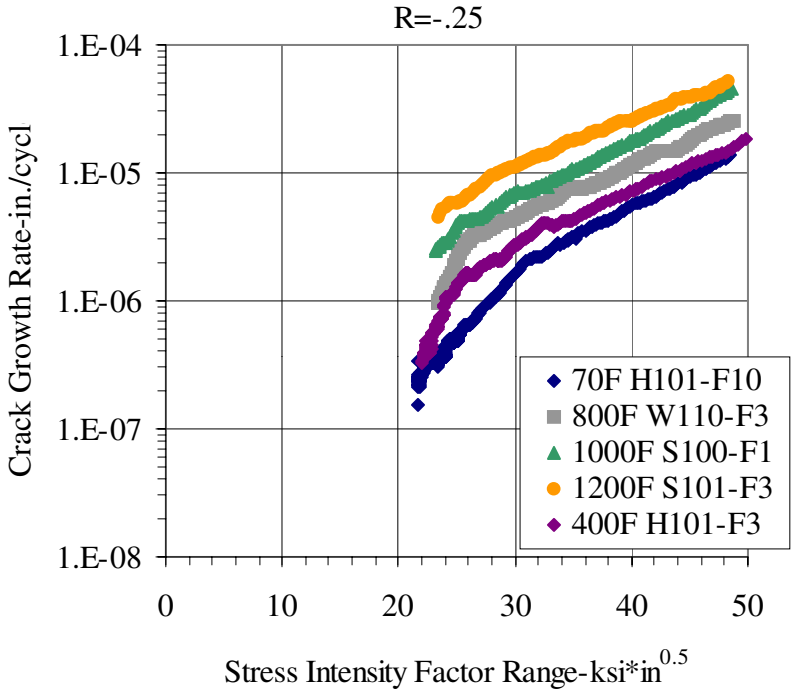

a. R_σ=-0.25

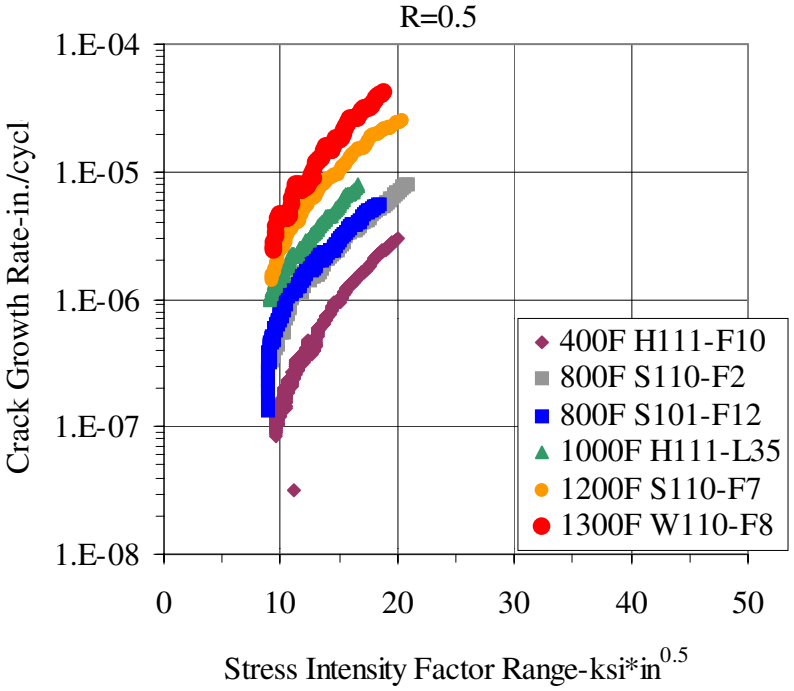

b. R_σ=0.5

Fig. 36. Typical cyclic fatigue crack growth test results, da/dn versus ΔK.

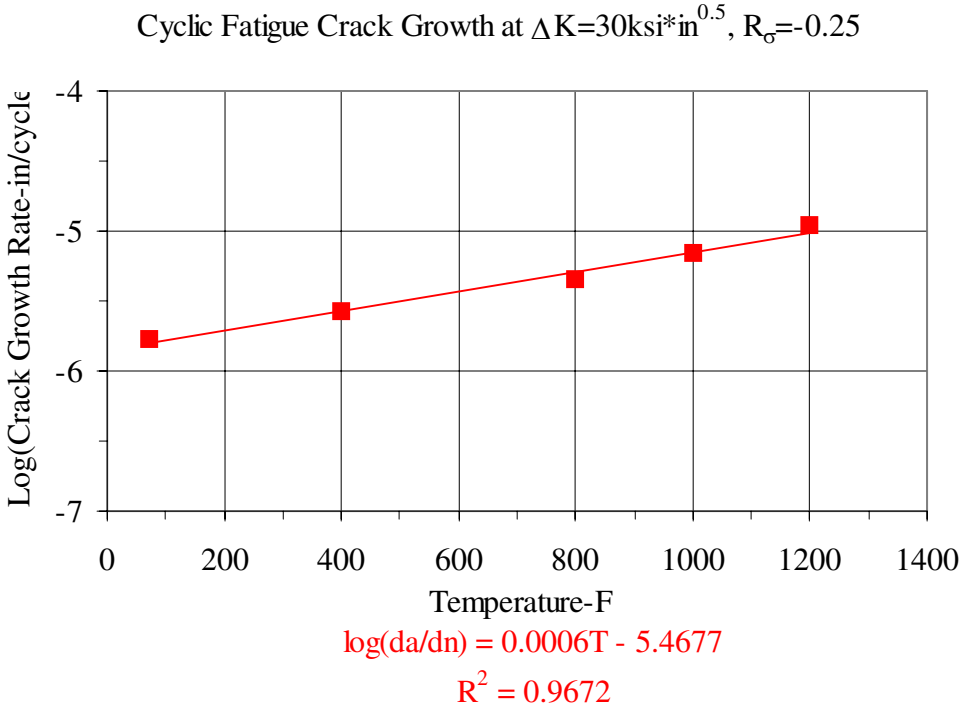

a.

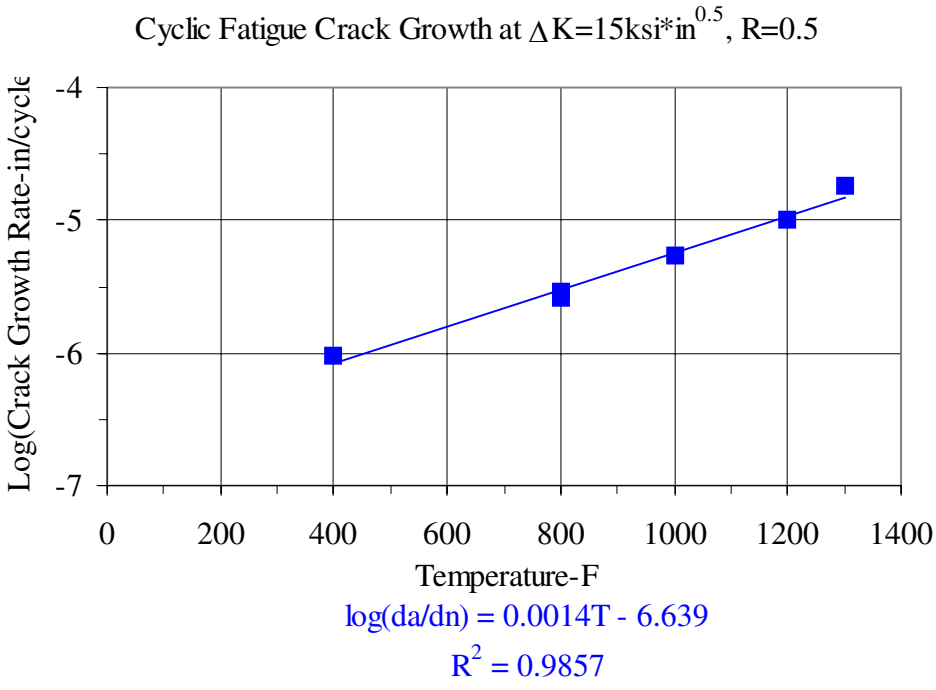

b.

Fig. 37. Comparison of cyclic fatigue crack growth rates versus temperature at stress ratios R_σ of a) –0.25; b) 0.5.

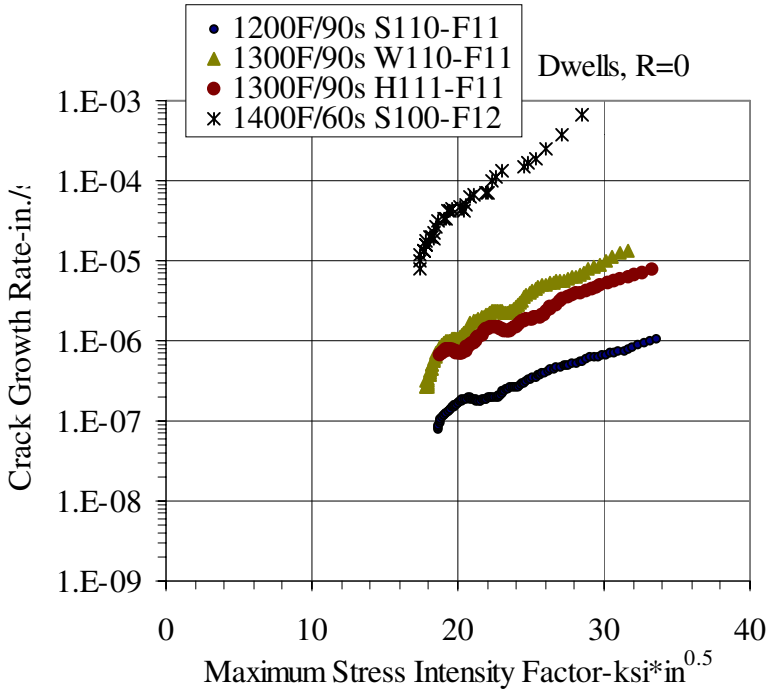

a.

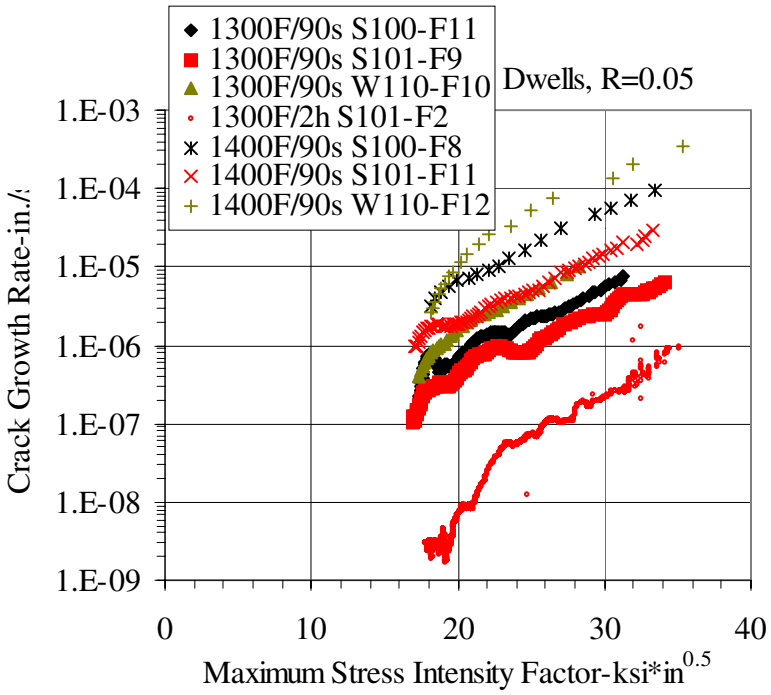

b.

Fig. 38. Typical dwell crack growth curves, da/dt versus $K_{max.}$, at a) R_σ=0; b) R_σ=0.05.

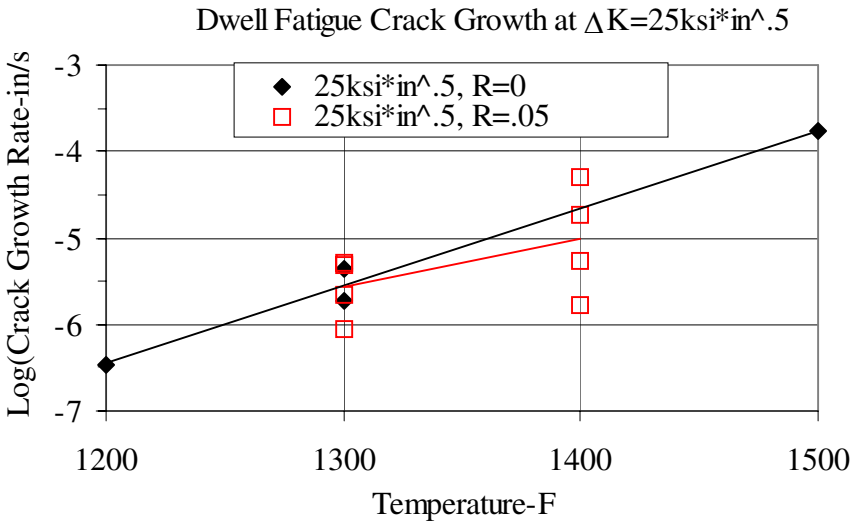

$\log(da/dt,R=0) = 0.009T - 17.217$

$R^2 = 0.9837$

$\log(da/dt,R=.05) = 0.0056T - 12.859$

$R^2 = 0.2776$

a.

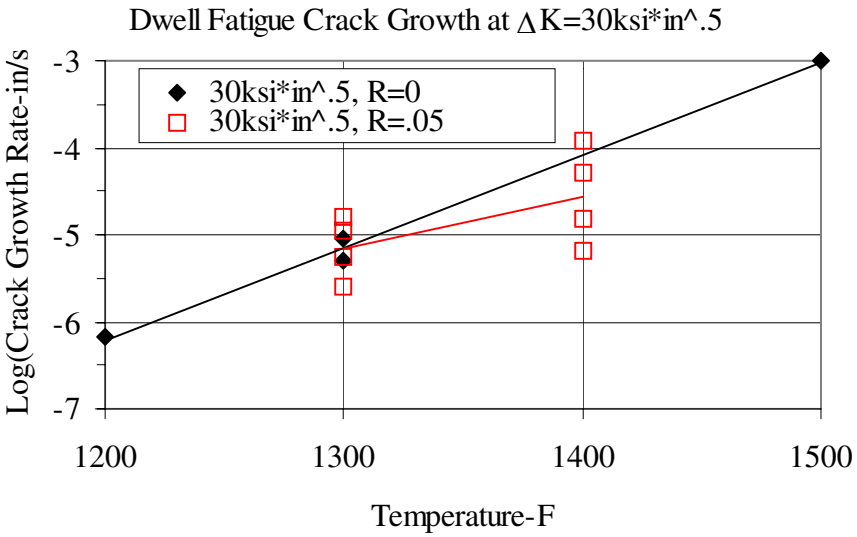

$\log(da/dt,R=0) = 0.0106T - 18.978$

$R^2 = 0.9934$

$\log(da/dt,R=.05) = 0.0059T - 12.879$

$R^2 = 0.3472$

b.

Fig. 39. Dwell fatigue crack growth rates versus temperature at different stress ratios R_σ at a) ΔK=25 and b) 30ksi*in$^{0.5}$.

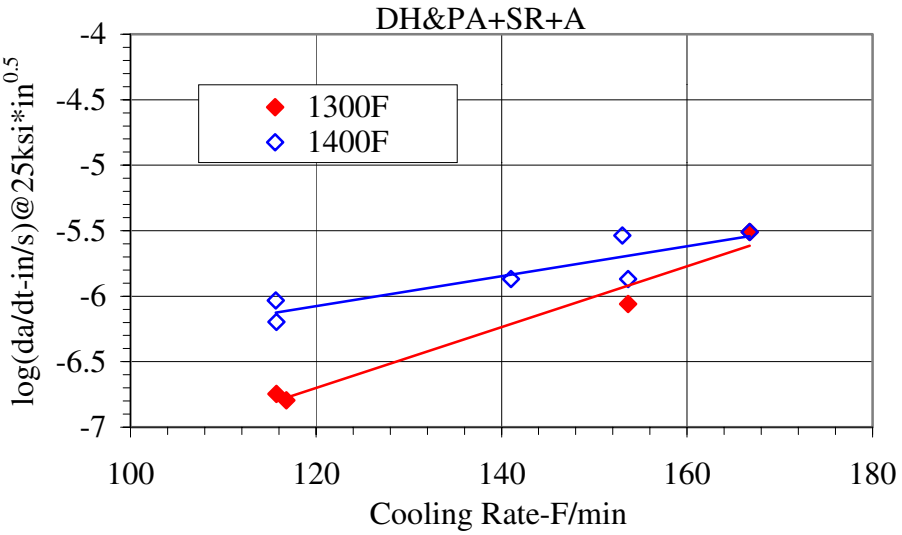

1400Flog(da/dt) = 0.0114CR - 7.4457 R^2 = 0.7984

1300Flog(da/dt) = 0.0233CR - 9.4929 R^2 = 0.9692

Fig. 40. Dwell fatigue crack growth rates at K_{max}=25 ksi*in$^{0.5}$ versus cooling rate at 1300 and 1400 °F for subscale disk material.

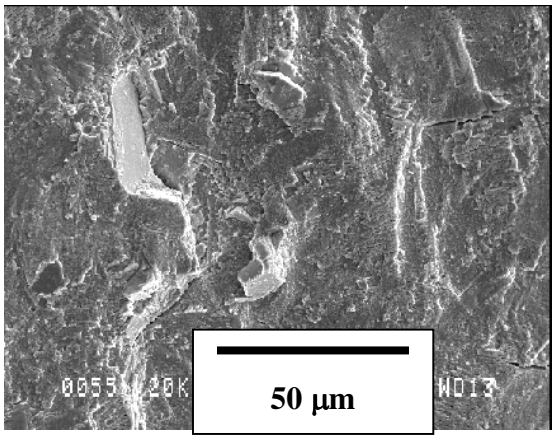

a.

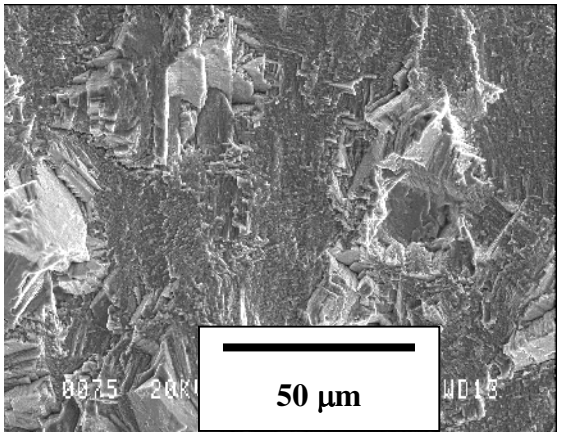

b.

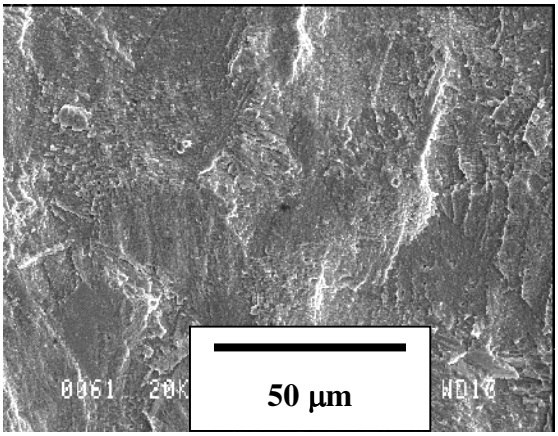

c.

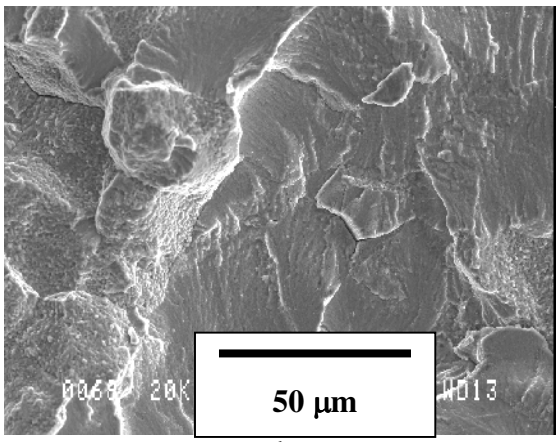

d.

Fig. 41. Typical cyclic crack growth modes: a. 400 °F, R=0.25; b. 800 °F, R=-1; c. 800 °F, R=0.25; d. 1300 °F, R=0.25.

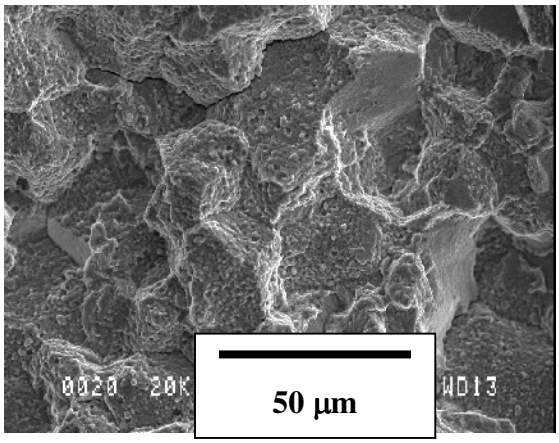

a.

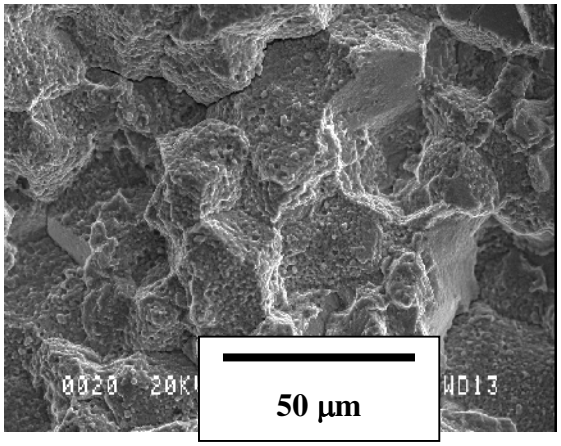

b.

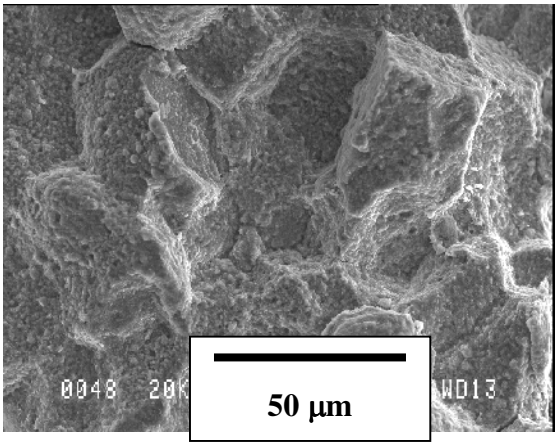

c.

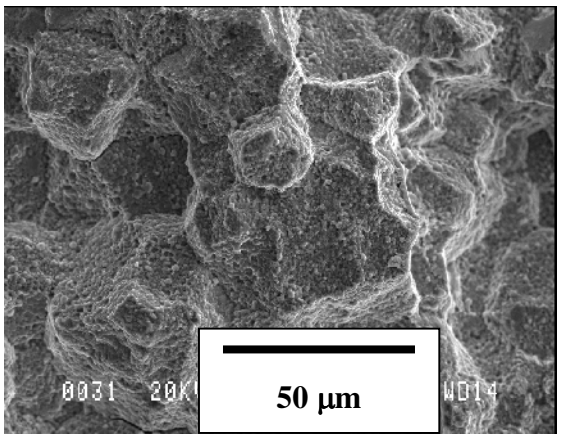

d.

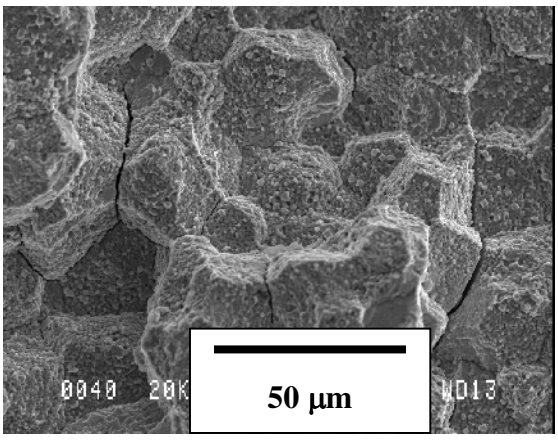

e.

Fig. 42. Typical dwell crack growth modes for: a. 1200 °F, 90 s dwell; b. 1300 °F, 90 s dwell; c. 1300 °F, 2 h dwell, d. 1400 °F, 90 s dwell, e. 1500 °F, 90 s dwell.

REPORT DOCUMENTATION PAGE

Form Approved
OMB No. 0704-0188

1. AGENCY USE ONLY (*Leave blank*)	2. REPORT DATE	3. REPORT TYPE AND DATES COVERED
	August 2002	Technical Memorandum

4. TITLE AND SUBTITLE

Characterization of the Temperature Capabilities of Advanced Disk Alloy ME3

5. FUNDING NUMBERS

WU–714–04–20–00

6. AUTHOR(S)

Timothy P. Gabb, Jack Telesman, Peter T. Kantzos, and Kenneth O'Connor

7. PERFORMING ORGANIZATION NAME(S) AND ADDRESS(ES)

National Aeronautics and Space Administration
John H. Glenn Research Center at Lewis Field
Cleveland, Ohio 44135–3191

8. PERFORMING ORGANIZATION REPORT NUMBER

E–13491

9. SPONSORING/MONITORING AGENCY NAME(S) AND ADDRESS(ES)

National Aeronautics and Space Administration
Washington, DC 20546–0001

10. SPONSORING/MONITORING AGENCY REPORT NUMBER

NASA TM—2002-211796

11. SUPPLEMENTARY NOTES

Timothy P. Gabb, Jack Telesman, and Kenneth O'Connor, NASA Glenn Research Center; Peter T. Kantzos, Ohio Aerospace Institute, Brook Park, Ohio 44142. Responsible person, Timothy P. Gabb, organization code 5120, 216–433–3272.

12a. DISTRIBUTION/AVAILABILITY STATEMENT

Unclassified - Unlimited
Subject Category: 07 Distribution: Nonstandard

Available electronically at http://gltrs.grc.nasa.gov

This publication is available from the NASA Center for AeroSpace Information, 301–621–0390.

12b. DISTRIBUTION CODE

13. ABSTRACT ***(Maximum 200 words)***

The successful development of an advanced powder metallurgy disk alloy, ME3, was initiated in the NASA High Speed Research/Enabling Propulsion Materials (HSR/EPM) Compressor/Turbine Disk program in cooperation with General Electric Engine Company and Pratt & Whitney Aircraft Engines. This alloy was designed using statistical screening and optimization of composition and processing variables to have extended durability at 1200 °F in large disks. Disks of this alloy were produced at the conclusion of the program using a realistic scaled-up disk shape and processing to enable demonstration of these properties. The objective of the Ultra-Efficient Engine Technologies disk program was to assess the mechanical properties of these ME3 disks as functions of temperature in order to estimate the maximum temperature capabilities of this advanced alloy. These disks were sectioned, machined into specimens, and extensively tested. Additional sub-scale disks and blanks were processed and selectively tested to explore the effects of several processing variations on mechanical properties. Results indicate the baseline ME3 alloy and process can produce 1300 to 1350 °F temperature capabilities, dependent on detailed disk and engine design property requirements.

14. SUBJECT TERMS

Gas turbine engines; Rotating disks; Heat resistant alloys; Fatigue (materials); Inclusions

15. NUMBER OF PAGES

57

16. PRICE CODE

17. SECURITY CLASSIFICATION OF REPORT	18. SECURITY CLASSIFICATION OF THIS PAGE	19. SECURITY CLASSIFICATION OF ABSTRACT	20. LIMITATION OF ABSTRACT
Unclassified	Unclassified	Unclassified	